

Modelling Theory and Applications of the Electromagnetic Vibrational Generator

Saha, C. R.

Published PDF deposited in [Curve](#) November 2016

Original citation:

Saha, C. R. (2011) 'Modelling Theory and Applications of the Electromagnetic Vibrational Generator' in Yen Kheng Tan (Ed). Sustainable Energy Harvesting Technologies - Past, Present and Future (pp: 55 - 109). InTech

<http://dx.doi.org/10.5772/27236>

DOI: 10.5772/27236

ISBN: 978-953-307-438-2

Publisher: Elsevier

Published under a CC BY 3.0 licence

(<https://creativecommons.org/licenses/by/3.0/>)

Copyright © and Moral Rights are retained by the author(s) and/ or other copyright owners. A copy can be downloaded for personal non-commercial research or study, without prior permission or charge. This item cannot be reproduced or quoted extensively from without first obtaining permission in writing from the copyright holder(s). The content must not be changed in any way or sold commercially in any format or medium without the formal permission of the copyright holders.

CURVE is the Institutional Repository for Coventry University

<http://curve.coventry.ac.uk/open>

Modelling Theory and Applications of the Electromagnetic Vibrational Generator

Chitta Ranjan Saha

*Score Project, School of Electrical & Electronic Engineering University of Nottingham,
Nottingham, NG7 2RD
UK*

1. Introduction

There is rapidly growing interest over the last decade on the topics of energy harvesting devices as a means to provide an alternative to batteries as a power source for medical implants, embedded sensor applications such as buildings or in difficult to access or remote places where wired power supplies would be difficult [1-13]. There are several possible sources of ambient energy including vibrational, solar, thermal gradients, acoustic, RF, etc that can be used to power the sensor modules or portable electronic devices. The most promising ambient energy sources of these are solar, thermo-electric and vibrational. A significant amount of research has already been done in this area over the past few years and several energy scavenger products are already available in the market such as the solar calculator, thermoelectric wristwatch and wireless push button switches etc. The Solar energy is a mature technology and represents a very straight forward approach to generate energy from ambient light. However, solar cell is not cost effective and devices using solar cell need larger areas which would not be compatible with small MEMS powering. Furthermore sufficient sunlight is necessary which also limits the application areas. In thermoelectric generators, large thermal gradients are essential to generate practical levels of voltage and power. It would be very difficult to get more than 10°C in a MEMS compatible device. On the other hand, vibrational energy scavenger could be a reliable option for autonomous sensor modules or body-worn sensor, in automotive, industrial machine monitoring or other applications where ambient vibrational energy is available. This vibrational energy can be converted into electrical energy using three different principles: electromagnetic, electrostatic and piezoelectric.

The modelling theory of the electromagnetic (EM) vibrational generator (energy scavenger) and its applications are main objective in this chapter in order to understand the limitations of the EM energy harvesting device and how to increase voltage and power level for a specific application. Initially, this chapter gives the basic working principles of vibrational energy harvester and electrical machines. Then it will provide the modelling and optimization theory of the linear EM vibrational energy scavenger and discuss the analytical equations of each modelling parameter. Thereafter, this chapter presents the few macro scale cantilever prototypes which have been built and tested. Their measured results are discussed and analysed with the theory in order to see the accuracy of the model. It will also investigate the possible applications of the vibrational energy harvester. A prototype of the

magnetic spring generator which has been built and tested for human body motion is presented and discussed the advantages of this structure. Finally we will present a prototype of optimized cantilever micro generator which has been built and integrated with the autonomous sensor module for machine monitoring application. The measured results of the real prototypes will provide the depth understanding of the readers what level of voltage and power could be harvested from the macro and micro level EM energy harvester and whether micro or macro device would be suitable for particular applications. The next section will give the brief overview of the working principle of the vibrational energy harvesters.

1.1 Kinetic/vibrational energy harvesting

Kinetic energy is the energy associated with the motion of an object. This includes vibrational motion, rotational motion and translational motion. The kinetic energy depends on two variables, the mass of the moving object (m) and the speed (U) of the object and is defined by [14];

$$K.E = \frac{1}{2} m U^2 \quad (1)$$

Kinetic energy is a scalar quantity and it is directly proportional to the square of its speed. In kinetic energy-harvesting, energy can be extracted from ambient mechanical vibrations using either the movement of a mass object or the deformation of the harvesting device. The basic operating principle of ac generator or alternator or EM harvester can be expressed using the energy flow diagram shown in Figure 1. When this external mechanical vibration or force is sufficient enough to overcome the mechanical damping force then the mass component of the energy harvesting devices to move or oscillate. This mechanical energy can be converted into electrical energy by means of an electric field (electrostatic), magnetic field (electromagnetic) or strain on a piezoelectric material, which are commonly known as electromechanical energy conversion principles. There also exists magnetostrictive energy harvesting devices which combine two principles: electromagnetic and piezoelectric.

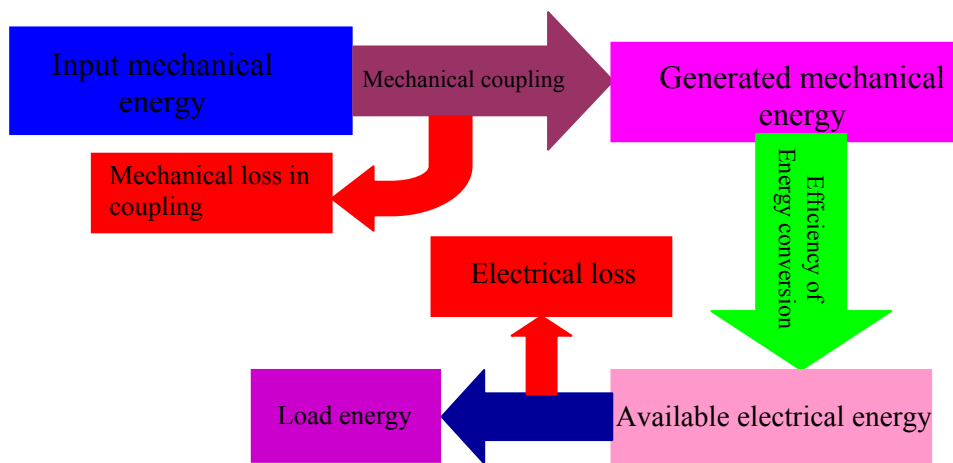


Fig. 1. Energy flow diagram of mechanical to electrical energy conversion principle.

Depending on the nature of the mechanical force, the generator can be classified in three categories: rotational generators, linear generators and deformation structure generators. The micro and macro scale linear or EM rotational generator, which is commonly known as an inertia generator in energy harvesting areas, will be investigated. Before introducing the EM energy harvester it is necessary to give a brief overview of the electrical machines such as transformer, motor and generator. Also the study of magnetic circuits is important since the operation of the EM energy harvester could be easily analyzed using the behavior of the magnetic fields. The next section will present the basic concepts of the electrical machines in order to understand the operating principle of the electromagnetic machines.

1.2 Concepts of electrical machine

An electrical machine is a electromechanical device that can convert either electrical energy to mechanical energy (known as a motor) or mechanical energy to electrical energy (known as generator). When such a device generates power in both directions it can be used as either a generator or a motor. The process of the electromechanical energy conversion normally involves the interaction of electric circuits and magnetic fields and the associated mechanical movement. This movement could be either rotational or linear due to forces arising between the fixed and the moving parts of the machine when we describe them as a rotational or linear machine. Another closely- related device is the transformer, which converts ac electrical energy at one voltage level to ac electrical energy at another voltage level. These three types of devices are very important in our everyday lives and sometimes such energy conversion devices are called transducer. One of the common factors between these machines is that they make use of magnetic fields to convert one form of energy to another. How these magnetic fields are used in such devices can be described by four basic principles [15-17];

1. A magnetic field will be produced surrounding a current-carrying conductor.
2. A time-changing magnetic field induces a voltage in a coil when it passes through it, which is called transformer action.
3. A current carrying conductor experiences a force in the presence of a magnetic field; this is known as motor action.
4. When a conductor such as copper wire moves in the magnetic field, a voltage will be induced between the conductor terminals; this is known as generator action.

The fourth principle is commonly known as Faraday's electromagnetic induction principle which has a wide range of applications, especially in power generation and power transmission theory. The following section will highlight the key components of the magnetic circuits since the magnetic field analysis is required to predict the performance of the electromagnetic device.

1.3 Magnetic materials and permanent magnet circuit model

Magnets are made from the magnetic materials and magnetic substances which consist of different metallic alloys. The magnetic materials are classified according to the nature of its relative permeability (μ_r) which is actually related to the internal atomic structure of the material and how much magnetization occurs within material. There are three categories the magnetic materials can be classified such as ferromagnetic materials, paramagnetic

materials and diamagnetic materials. It is necessary to know the few quantities of the magnetic material such as magnetic flux density, B ($T = \text{wb}/\text{m}^2$), the magnetizing force, H (A/m) and the magnetic flux, ϕ (wb). The relation between the magnetic flux density and the magnetizing force can be defined by;

$$B = \mu H = \mu_r \mu_0 H \quad (2)$$

Where μ (H/m) is the material permeability, μ_r is the relative permeability and μ_0 is the permeability in free space $4\pi \times 10^{-7} \text{ H}/\text{m}$.

1.3.1 Ferromagnetic materials

The ferromagnetic materials have very large positive values of magnetic permeability and they exhibit a strong attraction to magnetic fields and are able to retain their magnetic properties after the external field has been removed. The relative permeability of ferromagnetic material could be a few hundred to a few thousand and they are highly nonlinear. Ferromagnetic materials those are easily magnetized called soft magnetic materials such as soft iron, silicon steel, soft ferrites, nickel-iron alloys etc. Soft magnetic materials have a steeply rising magnetization curve, relatively small and narrow hysteresis loop as shown in figure 2 (a). They are normally used in inductors, motors, actuators, transformer, sonar equipments and radars. Those ferromagnetic materials have a gradually rising magnetization curve, large hysteresis loop area and large energy loss for each cycle of magnetization as shown in figure 2 (b) called hard magnet or permanent magnet. Alnico, Ceramic, Rare-earth, Iron-chromium-Cobalt, Neodymium-Iron-boron etc are few examples of permanent magnet materials. The more details of the Hysteresis loop (B - H curve) is explained in different literatures [16-17].

1.3.2 Paramagnetic materials

The paramagnetic materials have small, positive values of magnetic permeability to magnetic fields. These materials are weakly attracted by the magnets when placed in a magnetic field and the materials could not retain the magnetic properties when the external field is removed. Potassium, aluminum, palladium, molybdenum, lithium, copper sulphate etc are common paramagnetic materials.

1.3.3 Diamagnetic materials

The diamagnetic materials have a weak, negative magnetic permeability to magnetic fields. Diamagnetic materials are slightly repelled by the magnets when placed in a magnetic field and the material does not retain the magnetic properties when the external field is removed. The examples of diamagnetic materials are bismuth, copper, diamond, gold etc.

Since the permanent magnet will be used to build the prototype of the electromagnetic vibrational power generator and it is necessary to understand the air gap flux density between magnet and coil. The magnetic excitation is supplied by permanent magnets which are used in all electromagnetic energy conversion devices and the air gap magnetic field density provides valuable information in evaluating the performance of any permanent

magnet machine. Most designers use simplified analytical models of magnetic fields in the early stage design and then use FEA in the second stage of the design for better performance evaluation. For this work, rectangular- shaped magnets are assumed. A method for calculating the field at any point due to a rectangular magnet has been presented in [18]. Each magnet has eight corners and each corner flux density is equal to the remanent (B_r) of the magnet.

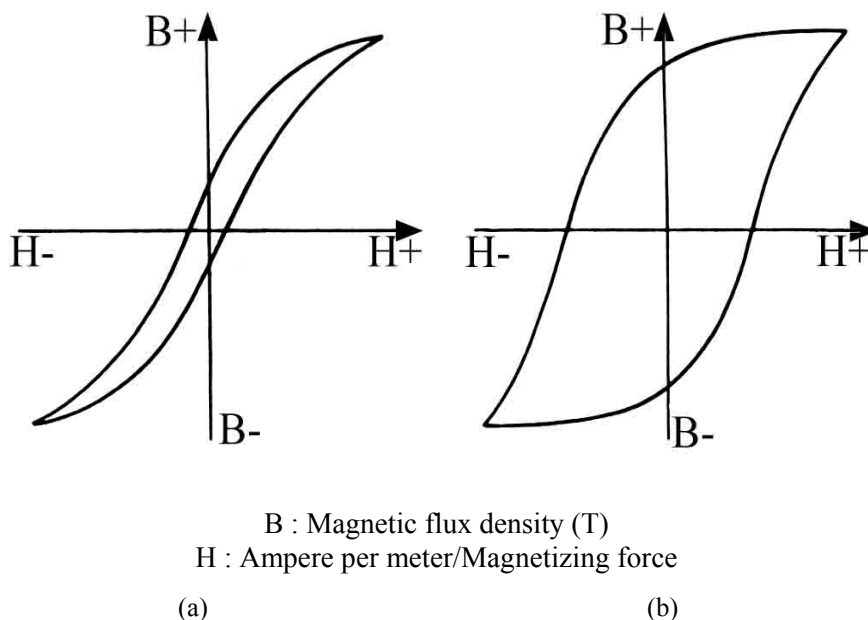


Fig. 2. Hysteresis loop (a) Soft magnetic materials (b) Hard magnetic materials.

Since the magnet has two opposite polarities, the remanent would be positive and negative consecutively as shown in figure 3. Suppose one corner co-ordinate is (x_k, y_k, z_k) with remanent ($-B_r$) and the flux density at a point $M(x, y, z)$ outside the magnet can be calculated [18] from the following equation,

$$B_{zk} = -B_r \arctan\left(\frac{x_r y_r}{z_r \sqrt{x_r^2 + y_r^2 + z_r^2}}\right) \quad (3)$$

Where B_{zk} is the flux density in the magnetization direction and $x_r = x - x_k$, $y_r = y - y_k$ and $z_r = z - z_k$. The total flux density $M(x, y, z)$ would be the summation of the eight corner flux densities.

Now we will discuss the magnetic circuit model of the permanent magnet. The second quadrant of the hysteresis loop is very valuable to describe the demagnetization characteristic of the permanent magnet. Figure 4 shows the linear demagnetization curve of the different permanent magnets [17-19]. Let consider the uniform cross sectional area and

length of permanent magnet are A_p and l_p respectively as shown in figure 5. The intersection of the loop with the horizontal axis (H) is known as the coercive force, H_c and the vertical axis (B) is known as the remanent flux density (B_r) or residual flux density. The linear demagnetization curve can be defined by;

$$B_p = \frac{B_r}{H_c}(H_p + H_c) = \mu_p(H_p + H_c) \quad (4)$$

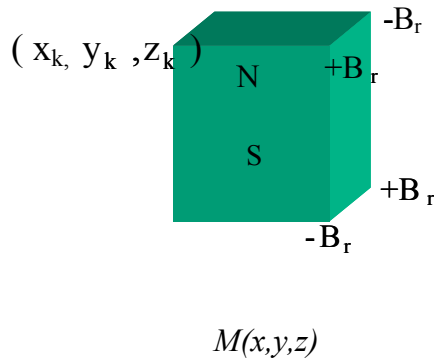


Fig. 3. Magnet flux density calculation

Where $\mu_p = \frac{B_r}{H_c}$ is the permanent magnet permeability. The electrical analogy of the magnetic components for flux linkage (ϕ) as current (I), the magnetomotive force (F_p) as a voltage source (E) and the magnetic reluctance as the resistance. The voltage drop across the magnet can be defined as [19];

$$H_p l_p = \frac{l_p}{\mu_p A_p} \phi_p - H_c l_p = \Re_p \phi_p - F_p \quad (5)$$

Where \Re_p is the magnetic reluctance of the permanent magnet, ϕ_p is the flux linkage and F_p is the magnetomotive force of the permanent magnet.

There is non linear demagnetization curve of the permanent magnet, linear magnetic circuit is still valid however the magnetic permeability would be;

$$\mu_p = \frac{B_p}{H_p + H_c} \quad (6)$$

The non linear magnetic circuit model of the permanent magnet can be represented in the figure 6. It can be seen from figure 7 that if the external magnetic field (H_{ex}) applied, the magnet operating point (H_p, B_p) would not move along the non-linear demagnetization curve, it simply moves along the centre line of the minor loop.

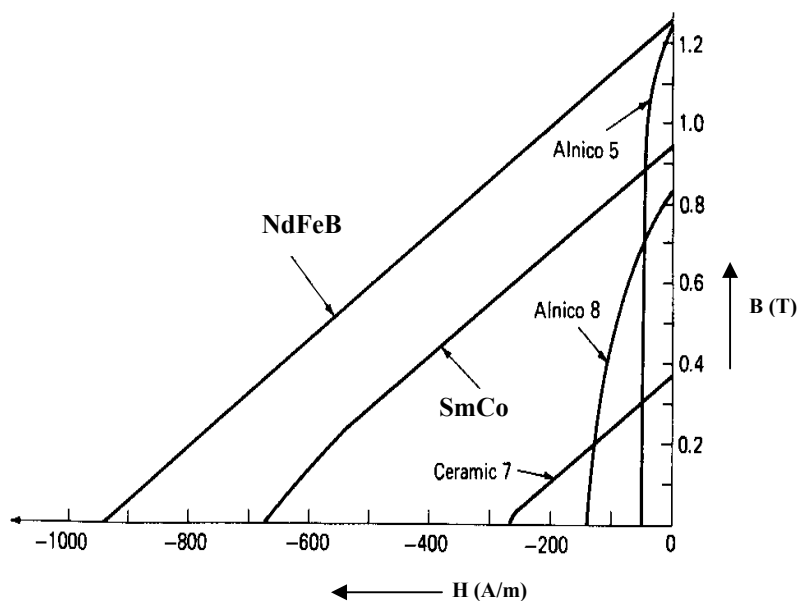


Fig. 4. Demagnetization curve of the permanent magnet [19]

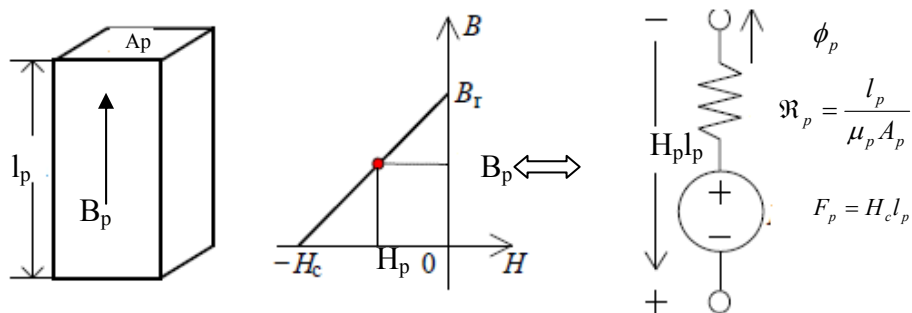


Fig. 5. Linear magnet circuit model of the permanent magnet.

where V is the generated voltage/induced emf and ϕ is the flux linkage.

If we consider the case where a coil moves in the x direction through a magnetic field or flux density B where B field varies along the coil movement, then the voltage can be expressed as:

$$V = \frac{d\phi}{dx} \frac{dx}{dt} \quad (8)$$

The flux linkage depends on the magnet and coil parameters and the air gap flux density between the magnet and coil. The shape of the air gap flux density could vary with the magnetic structure of the generator. The situation for vibrational generators can be approximated by a coil moving in a single direction through a magnetic field which varies in the direction of movement, as depicted in Figure 8. The flux linkage through a single turn conductor which encircles a surface area ($dA=dx dy$), and which is positioned in a B field which varies with x but not y , can be expressed as;

$$\phi = \iint B \cdot dA = \iint B \cdot dx dy = \Delta y \int_0^{\Delta x} B(x) dx$$

and the flux linkage gradient is therefore;

$$\frac{d\phi}{dx} = \Delta y [B(\Delta x) - B(0)] \quad (9)$$

where $B(0)$ and $B(\Delta x)$ are the flux density at the $x=0$ position and the $x=\Delta x$ position.

The expression for the generated voltage as the product of the flux linkage gradient and the velocity is important for understanding the operation of the vibrational generator.

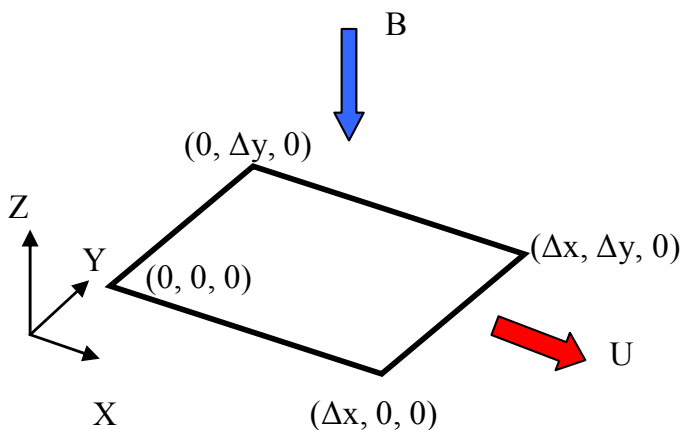


Fig. 8. Movement of a conductor in a position varying magnetic field.

1.4.1 Loudspeaker type vibrational generator

Figure 9 shows the schematic of a typical moving coil loudspeaker type linear generator. The loudspeaker type generator consists of a moving coil inside a static magnetic field where the voice coil is connected to the cone and its suspension [20]. Normally the cone is made from carbon fibre, plasticized cloth or paper. The magnet assembly consists of front plate, back plate, yoke pole piece which are mainly made from low cost iron material and a large ferrite magnet. In the majority of loudspeaker designs the magnet height is longer than the coil height and the coil movement within the magnet height for full excursion. The flux density over the coil movement is constant for this kind of structure. The generated voltage would be;

$$V = BIU \quad (10)$$

Since the loudspeaker suspension is made from plastic, fibre or papers etc which are high loss material. Normally it is designed for small movement and will be flat response over the frequency range. The electromagnetic vibrational generator requires a particular frequency response with high efficiency.

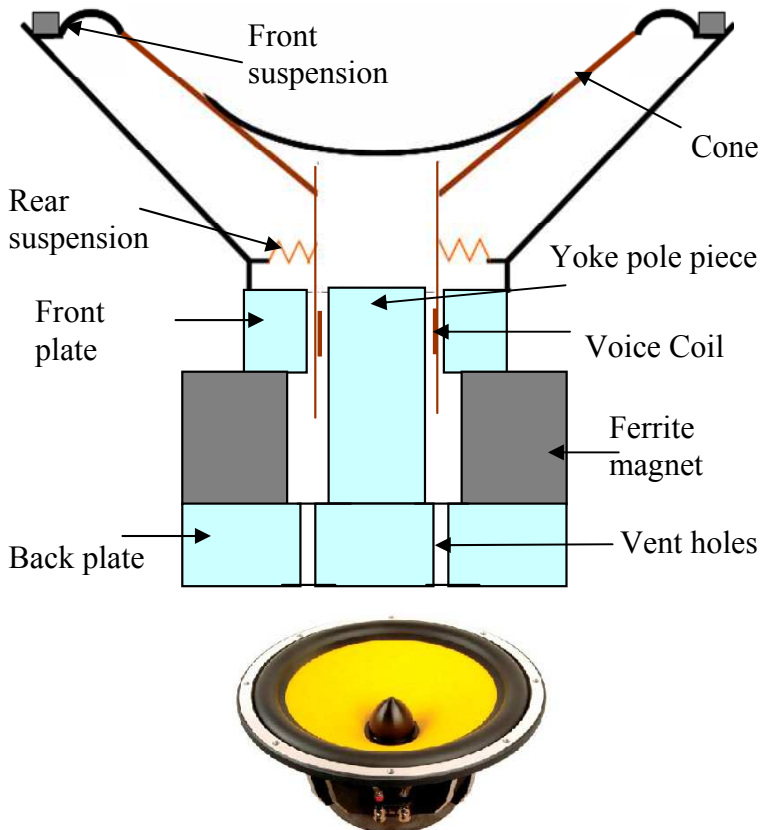


Fig. 9. Typical loudspeaker structure

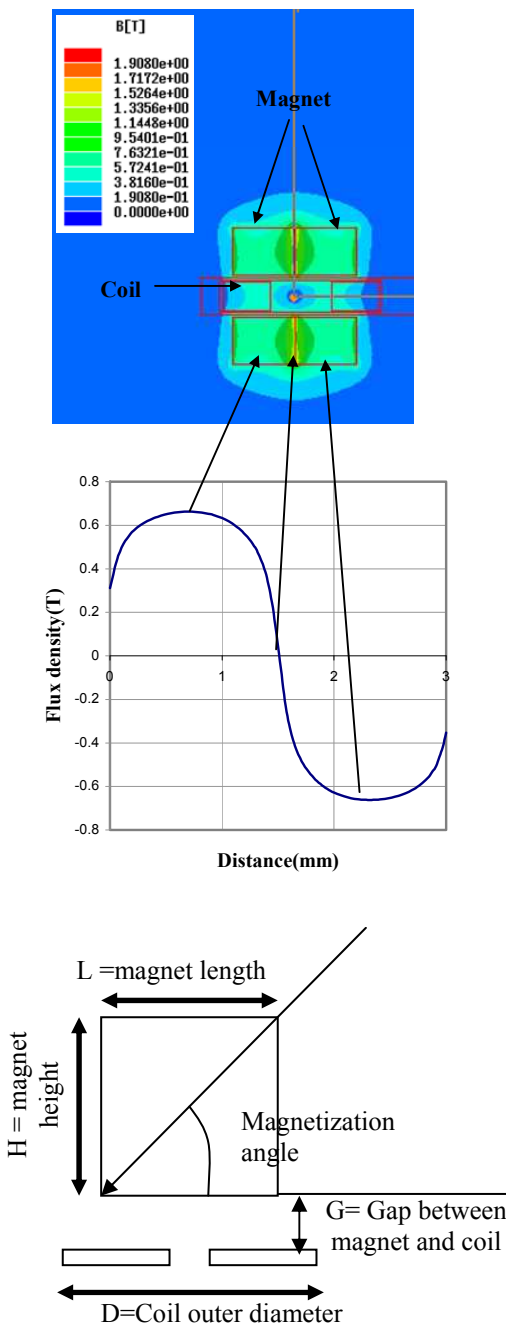


Fig. 10. Air gap flux density along the coil axis of the four magnets and single coil generator structure.

1.4.2 Four magnets vibrational generators

In this chapter rectangular shape four magnets and single coil generator structure is used for macro and micro scale prototype to verify the modeling theory. Figure 10 shows finite element simulation results of the air gap flux density (B) of the four magnet generator structure along the coil axis. This four magnet generator has several advantages. Since the coil is placed in the gap between upper and lower magnets, the field experienced by this coil is relatively large. In addition, the field is mostly perpendicular to the coil so that it contributes efficiently to the generated voltage. A four-magnets arrangement is used so as to produce two pole pairs. In its resting position, the coil is positioned mid-way between these pole pairs, i.e. half of the coil rests under one pole and half under the other. This is important as it means that the coil is subjected to a high flux gradient which should thus give rise to a relatively high voltage. It can be seen from this figure that the flux density is maximum at the mid position in each magnet and the flux density is zero between the mid points of the pole pairs.

It is fundamental to know the application before designing the generator. Need to consider the issues what level of acceleration or force and frequency are available and whether macro or micro size magnet and coil would generate sufficient power. Also what kind of generator structure such as magnet, coil and suspension would be suitable for the specific application? Finally how magnet and coil could be optimized to reduce cost and size for the specific application to deliver maximum power.

In the following section, we discuss the details of the model and the optimum condition for the generator.

1.5 Model of the electromagnetic vibrational generator

The basic vibrational energy harvester can be modeled as a second order mass damper and spring system [1-6]. It consists of a mass (m) mounted on a spring or a beam (k) which vibrates relative to a housing when subjected to an external vibrational force. For an electromagnetic generator mass may consist of the magnet itself or the coil. Figure 11 shows the typical structure of a generator as described by P.Glynne-Jones [21]. In this generator, two opposite polarity magnets were fixed in a gap at the free end of the cantilever and a wire-wound coil was placed in the gap between the magnets. When the external force is applied to the generator housing, the voltage would be generated in the coil terminal due to the relative displacement between magnets and coil. In order to have a model, it is important to develop the equations for the various generator parts such as the magnet parameters, the coil parameters, beam parameters and damping (D) parameters.

Figure 12 shows the schematic diagram of the electromagnetic generator. Variables z and y are the displacements of the generator mass and housing, respectively. It is assumed that movement of the housing is unaffected by the movement of the generator, since the moving mass (m) is much smaller than the mass of the generator housing. For a sinusoidal excitation, $y = Y_0 \sin(\omega t)$, where Y_0 is the vibration amplitude and ω is the frequency of vibration. The equation of motion for the mass relative to the housing at no load condition (no electromagnetic forces considered) can be defined [4-5] by the following equation,

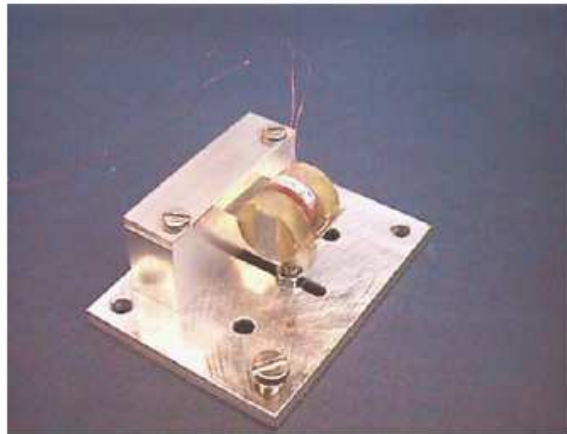


Fig. 11. Typical generator structure

$$m \frac{d^2 x}{dt^2} + D_p \frac{dx}{dt} + kx = -ma(t) = F_0 \sin \omega t \quad (11)$$

where m is the moving mass of the generator, x is the relative movement between the mass and the housing, D_p is the parasitic damping, and $F_0 = m\omega^2 a$. The parasitic damping of the generator is commonly known as mechanical loss and can consist of air resistance loss, surface friction loss, material hysteresis loss, etc. It depends on material properties, the size and shape of the generator, external force, frequency, and vibrational displacement. k is the beam spring constant where the natural resonant frequency ω_n is given by, $\omega_n = \sqrt{k/m}$. The steady state solution of equation (4) is the displacement for the no-load condition and is given by the following equation [4]:

$$x_{no-load} = \frac{F_0 \sin(\omega t - \phi)}{\sqrt{(k - m\omega^2)^2 + (D_p \omega)^2}} \text{ where, } \phi = \tan^{-1} \left(\frac{D_p \omega}{k - m\omega^2} \right) \quad (12)$$

This parasitic damping can be calculated from the open circuit quality factor and the damping ratio of the system, which can be expressed by;

$$Q_{oc} = \frac{m\omega_n}{D_p}, \quad \xi_{0c} = \frac{D_p}{2m\omega_n}$$

The damping ratio (ξ_{0c}) determines the qualitative behaviour of the system and it compares the time constant for decay of an oscillating system's amplitude to its oscillating period. The details of this parasitic damping and quality factor will be given later in this chapter.

It is well known that any mechanical, electrical or acoustic system always generates the maximum vibration amplitude at the resonance condition. Any system can have more than one resonance frequencies and resonance occurs when the system's natural frequency matches the frequency of oscillation of the external force.

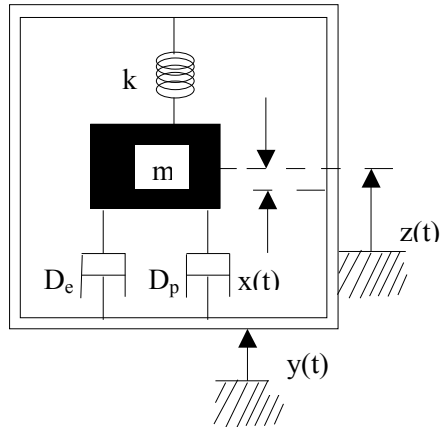


Fig. 12. Schematic representation of the vibrational generator.

The displacement at resonance ($\omega = \omega_n$) is given by;

$$x_{no-load} = \frac{-F_0 \cos(\omega_n t)}{D_p \omega_n} \quad (13)$$

and the phase angle, ϕ between displacement and the forcing signal is 90° .

When a load is connected to the generator coil terminal, an electromagnetic force will be generated between the magnet and the coil due to the current flow through the load; this opposes the movement of the generator [5]. Thus, the equation of motion of the generator mass includes an extra term due to the magnetic force and becomes;

$$m \frac{d^2 x}{dt^2} + D_p \frac{dx}{dt} + kx = F_0 \sin \omega t - F_{em} \quad (14)$$

where the F_{em} is the electromagnetic force.

The conductor moves along the X axis at velocity U in magnetic field B that varies with the position x as shown in Figure 2. In this case, the force experienced on the current-carrying conductors in the loop is;

$$F_{em} = \int IBdl = \int IB \cdot dx = I \left[\int_{(0,0,0)}^{(\Delta x, 0, 0)} B \cdot dx + \int_{(\Delta x, 0, 0)}^{(\Delta x, \Delta y, 0)} B \cdot dx + \int_{(\Delta x, \Delta y, 0)}^{(0, \Delta y, 0)} B \cdot dx + \int_{(0, \Delta y, 0)}^{(0, 0, 0)} B \cdot dx \right]$$

$$F_{em} = I [\Delta x \{B(\Delta x) - B(0)\} + \Delta y B(\Delta x) + \Delta x \{B(0) - B(\Delta x)\} - \Delta y B(\Delta x)] = I \Delta y (B(0) - B(\Delta x))$$

Using equation (3).

$$F_{em} = I \frac{d\phi}{dx}$$

If the magnetic field B is constant with the position x then, $F_{em} = BIl$ where l is the coil mean length.

In this chapter we will present the magnetic flux density (B) varies with the coil movement, so that

$$F_{em} = \frac{V}{R_c + R_l + j\omega L} \frac{d\phi}{dx} = \frac{1}{R_c + R_l + j\omega L} \left(\frac{d\phi}{dx} \right) \left(\frac{dx}{dt} \right) \left(\frac{d\phi}{dx} \right) = \frac{\left(\frac{d\phi}{dx} \right)^2}{R_c + R_l + j\omega L} \frac{dx}{dt}$$

where, V is the generated voltage, R_c is the coil resistance, L is the coil inductance, and R_l is the load resistance.

For an N turn coil, the total flux linkage gradient would be the summation of the individual turns flux linkage gradients. If the flux linkage gradient for each turn is equal then the electromagnetic force is given by;

$$F_{em} = \frac{N^2 \left(\frac{d\phi}{dx} \right)^2}{R_c + R_l + j\omega L} \frac{dx}{dt} = D_{em} \frac{dx}{dt}$$

Where the electromagnetic damping,

$$D_{em} = \frac{N^2 \left(\frac{d\phi}{dx} \right)^2}{R_c + j\omega L + R_l} \quad (15)$$

It can be seen from (15) that electromagnetic damping can be varied by changing the load resistance R_c , the coil parameters (N , R_c and L), magnet dimension and hence flux (ϕ) and the generator structure which influence $\frac{d\phi}{dx}$. Putting the electromagnetic force

($F_{em} = D_{em} \frac{dx}{dt}$) in equation (7) gives;

$$m \frac{d^2 x}{dt^2} + D_p \frac{dx}{dt} + D_{em} \frac{dx}{dt} + kx = F_0 \sin \omega t \quad (16)$$

The solution of equation (9) defines the displacement under electrical load condition and is given by the following equation,

$$x_{load} = \frac{F_0 \sin(\omega t - \theta)}{\sqrt{(k - m\omega^2) + [(D_p + D_{em})\omega]^2}} \quad (17)$$

Where $\theta = \tan^{-1} \left[\frac{(D_p + D_{em})\omega}{(k - m\omega^2)} \right]$

The displacement at resonance under load is therefore given by;

$$x_{load} = \frac{-F_0 \cos \omega t}{(D_p + D_{em})\omega} \quad (18)$$

1.5.1 Generated mechanical power

The instantaneous mechanical power associated with the moving mass under the electrical load condition is

$$\begin{aligned} P_{mech}(t) &= F(t) \cdot U(t) \\ &= F_0 \sin(\omega t) \frac{dx_{load}}{dt} \\ &= \frac{F_0^2 \sin^2(\omega t)}{(D_p + D_{em})} \text{ using equation (18)} \end{aligned}$$

Where $F(t)$ and $U(t)$ are the applied sinusoidal force and velocity of the moving mass, respectively, due to the sinusoidal movement. This corresponds to maximum mechanical power when $D_{em}=0$, i.e. at no load.

The average mechanical power is defined by,
$$P_{mech} = \frac{1}{T} \int_0^T \frac{F_0^2 \sin^2(\omega t)}{(D_p + D_{em})} dt = \frac{F_0^2}{2(D_p + D_{em})}$$

1.5.2 Generated electrical power and optimum damping condition

In a similar manner, the generated electrical power can be obtained from;

$$P_e(t) = F_{em} \cdot U(t) = D_{em} U^2(t)$$

The average electrical power can be obtained from,

$$P_e = \frac{1}{T} \int D_{em} \left(\frac{dx_{load}}{dt} \right)^2 dt \quad (19)$$

Taking the time derivative of equation (10) and putting the value in equation (12), we obtain

$$P_e = D_{em} \frac{(F_0 \omega)^2}{2[(k - m\omega^2)^2 + (D_p + D_{em})^2 \omega^2]} \quad (20)$$

The average electrical power generated at the resonance condition ($\omega=\omega_n$) is given by ;

$$P_e = D_{em} \frac{F_0^2}{2(D_p + D_{em})^2} \quad (21)$$

If the parasitic damping is assumed to be constant over the displacement range then the maximum electrical power generated can be obtained for the optimum electromagnetic

damping. At the resonance condition ($\omega=\omega_n$), the maximum electrical power and optimum electromagnetic damping can be found by setting $\frac{dP_e}{dD_{em}}=0$ and solving for D_{em} . This gives the maximum power as;

$$P_{\max} = \frac{F_0^2}{8D_p} \quad (22)$$

This occurs when $D_{em} = D_p$, which is the optimum electromagnetic damping at the resonance condition. Putting the value $D_{em} = D_p$ in equation (8) gives the displacement at the optimum load.

$$x_{load} = \frac{x_{no-load}}{2} \quad (23)$$

Thus, at the resonance condition, maximum power will be generated when the load displacement is half of the no-load displacement.

1.5.3 Maximum power and maximum efficiency

The maximum efficiency and maximum power depends on the external driving force and the design issues of the electromagnetic generators. If the driving force is fixed over the variation of the load and the electromagnetic damping or force factor (Bl) is significantly high compare to mechanical damping factor then the maximum power and maximum efficiency will appear at the same load resistance. Otherwise when the driving force is not constant and the force factor is significantly low or not high enough compare to mechanical damping or any of these situations the maximum power and the maximum efficiency will occur on different load resistance values.

1.5.4 Optimum load resistance for maximum generated electrical power

It is always desirable to operate the device at high efficiency and for an electrical generator, it is also desired to deliver maximum power to the load at a relatively high voltage. In an electromagnetic generator, most of the electrical power loss appears due to the coil's internal resistance. Here we will investigate what would be the optimum load resistance in order to get maximum power to the load. The electrical power and voltage lost in the coil internal resistance under these conditions are also investigated.

The optimum power condition occurs for $D_{em} = D_p$, which can be written as,

$$N^2 \left(\frac{d\phi}{dx} \right)^2 \frac{1}{R_c + R_l + j\omega L} = D_p$$

In general, for less than 1 kHz frequency, $j\omega L$ can be neglected compared to R_c . Therefore, rearranging to get R_l , gives the optimum load resistance which ensures maximum generated electrical power namely,

$$R_l = \frac{N^2 \left(\frac{d\phi}{dx} \right)^2}{D_p} - R_c \quad (24)$$

The above equation indicates that an optimum load resistance may not be positive if the first term on the right side is less than R_c . This can occur if either the parasitic damping factor (D_p) is large, the flux linkage gradient ($\frac{d\phi}{dx}$) is low, or the coil resistance is high. Since it is therefore not always possible to achieve the optimum condition by adjusting the load resistance, then it is worth considering the optimum conditions in various situations.

Very Low Electromagnetic damping case ($D_{em} \ll D_p$) :

In the low electromagnetic damping case, due to low $\frac{d\phi}{dx}$ or high R_c , it is impossible to make the electromagnetic damping equal to the parasitic damping. If the electromagnetic damping for the short circuit condition is much less than the parasitic damping ($D_{em} \ll D_p$), there will be no significant change in displacement between the no-load and load conditions. In this case, the maximum power will be delivered to the load when the load resistance is matched to the coil resistance. Since the load resistance has to be equal to the generator internal resistance, 50% of the voltage and power will be lost in the generator internal resistance and the generator efficiency is likely to be very low.

Limitation of the model ($D_p < D_{em} < D_p$) :

If the electromagnetic damping for very low load resistance is only slightly less than D_p , but can not be made equal to D_p then there will be a change in displacement between the no-load and load condition but the optimum load resistance at maximum generated power condition cannot be analyzed by the modeling equation. However, the optimum load resistance to maximize the load power condition, as opposed to the generated power could be determined from the modeling equation.

1.5.5 Optimum load resistance for maximum load power

In order to find the optimum resistance which maximizes the load power, we can take the expression for the load power and differentiate with respect to the load resistance.

The average generated electrical power is:

$$P_e = D_{em} \frac{F_0^2}{2(D_p + D_{em})^2}$$

The average load power would therefore be:

$$P_{load} = \frac{R_l}{R_c + R_l} \left[\frac{D_{em} F_0^2}{2(D_p + D_{em})^2} \right]$$

Inserting the expression for D_{em} from equation (15) and rearranging gives:

$$P_{load} = \frac{R_l F_o^2 N^2 \left(\frac{d\phi}{dx}\right)^2}{2[D_p(R_c + R_l) + \left(\frac{d\phi}{dx}\right)^2 N^2]^2}$$

Now the optimum load resistance at the maximum load power can be found by setting $\frac{dP_l}{dR_l} = 0$, which gives:

$$R_{lopt} = R_c + \frac{N^2 \left(\frac{d\phi}{dx}\right)^2}{D_p} \quad (25)$$

In order to understand the optimum conditions of the generators, the displacement and load power were calculated theoretically for different parasitic damping factors. The parasitic damping, EM damping, displacement, generated voltage, the load power and the optimum load resistance at maximum load power were calculated by the following equations using the values in Table 1;

$$D_p = \frac{m\omega_n}{Q_{oc}}, \quad D_{em} = N^2 \frac{\left(\frac{d\phi}{dx}\right)^2}{R_c + R_l}, \quad x_{load} = \frac{ma}{(D_p + D_{em})\omega_n}, \quad V = \frac{d\phi}{dx} \frac{dx}{dt},$$

$$P_l = \frac{(VR_l)^2}{2R_l(R_c + R_l)^2}, \quad R_{lopt} = R_c + \frac{N^2 \left(\frac{d\phi}{dx}\right)^2}{D_p}$$

Parameters	value
N	500
Coil internal resistance, R_c (Ω)	33
Flux linkage gradient, $\frac{d\phi}{dx}$ (wb/m)	1e-03
Frequency, f (Hz)	1000
Acceleration, a (m/s^2)	9.81
Mass (kg)	1.97e-03

Table 1. Assumed parameters of the Generators

Figure 13 shows the displacement vs load resistance, assuming different values of open circuit quality factor (Q_{oc}) for a 500 turns coil. It can be seen from the graphs that the significant variation of displacement for $Q_{oc}=10000$ ($D_p=0.0012$ N.s/m) is due to the change in the load resistance value. Figures 14, 15 and 16 show the corresponding load power and damping factor vs load resistance. For $Q_{oc}=10000$, the maximum power is generated and

transferred to the load when the electromagnetic damping is equal to the parasitic damping; this agrees with the theoretical model. In this case, the electromagnetic damping for very low load resistance is almost 6 times higher ($D_{em} \gg D_p$) than the parasitic damping factor. Since the optimum R_{load} is much greater than R_{coil} , 90% of the generated electrical power is delivered to the optimum load resistance value. The optimum load resistance at maximum load power is 255Ω , which agrees with the theoretical equation (25).

For $Q_{oc}=1000$ there is some variation of displacement for changing load resistance values but it is not as significant as for the $Q_{oc}=10000$ case. In this case, electromagnetic damping for low load resistance is lower than parasitic damping ($D_{em} < D_p$) but not significantly lower. In this situation the optimum condition for the generated maximum power could not be defined by the modeling equation but the optimum load resistance at maximum load power is 55 which agrees well with theoretical equation (25). The optimum load resistance tends to be close in value to the coil resistance.

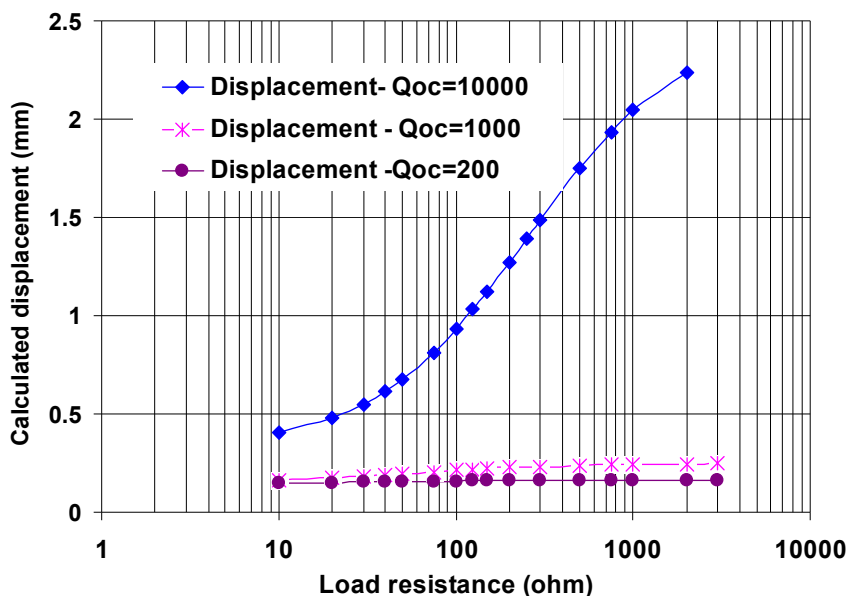


Fig. 13. Variation of displacement for different quality factors for $N = 500$ turns coil generator

For $Q_{oc}=200$, there is no variation of displacement for changing load resistance values and the electromagnetic damping for all load resistances is significantly lower than the parasitic damping factor ($D_p \gg D_{em}$). In this case the maximum power is delivered to the load when the load resistance equals the coil resistance. It is assumed in the above that the parasitic damping is almost constant with the displacement. However, this parasitic damping can depend on the generator structure and the properties of the spring material such as friction, material loss etc.

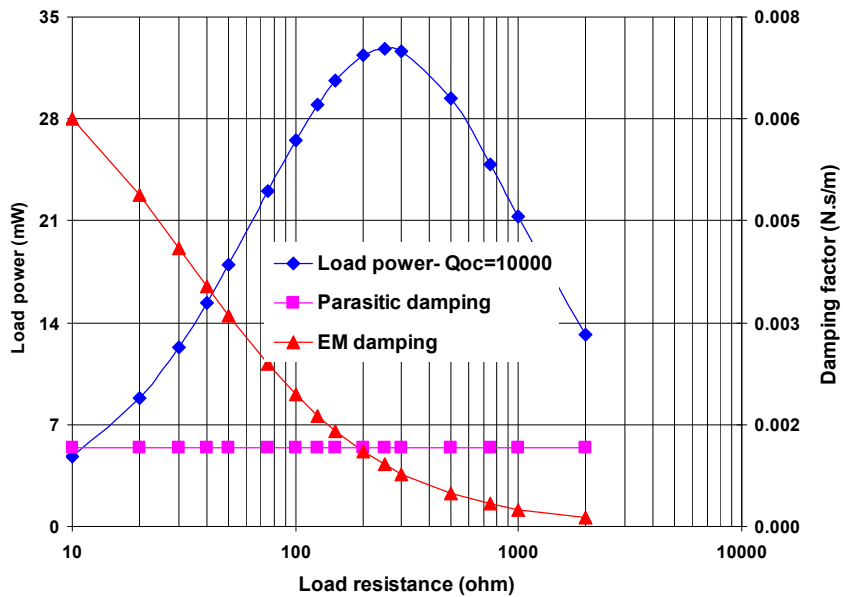


Fig. 14. Calculated load power and damping factor for $Q_{oc} = 10000$ and $N = 500$ turns coil generator.

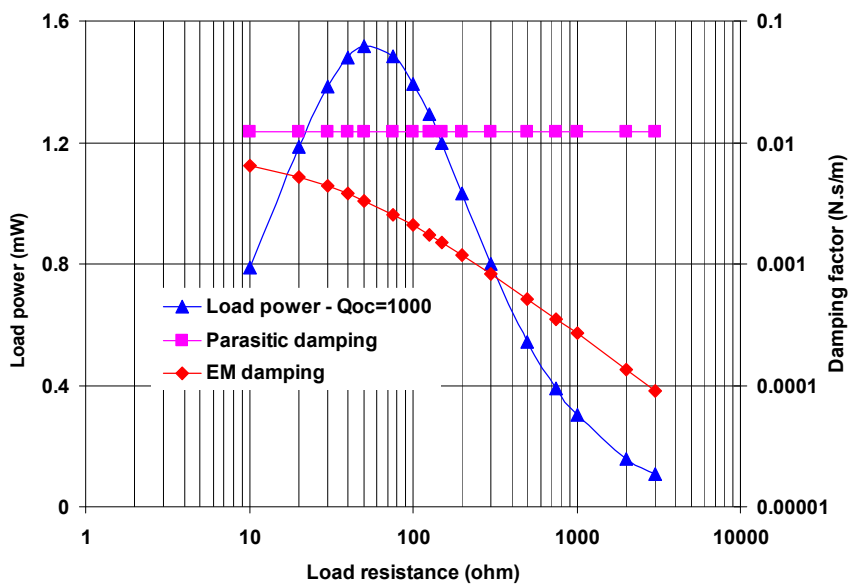


Fig. 15. Calculated load power and damping factor for $Q_{oc} = 1000$ and $N = 500$ turns coil generator.

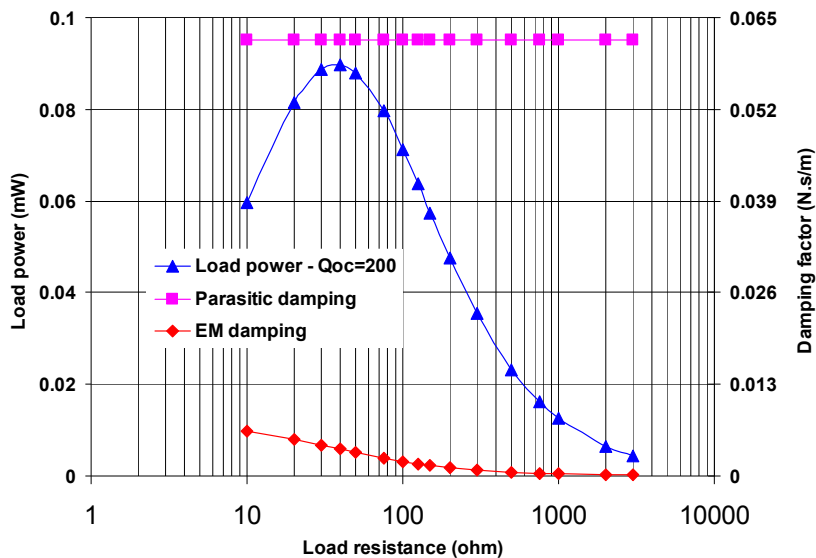


Fig. 16. Calculated load power and damping factor for $Q_{oc} = 200$ and $N=500$ turns coil generator.

1.6 Parasitic or mechanical damping and open circuit quality factor

The parasitic damper model of the mechanical beam in the electromagnetic vibrational generator structure is considered as a linear viscous damper [22-27]. The parasitic damping therefore determines the open-circuit or un-loaded quality factor which can be expressed as;

$$Q_p = \frac{m\omega_n}{D_p} = \frac{1}{2\zeta_p} = \frac{f_n}{f_2 - f_1} \quad (26)$$

Where ζ_p is the parasitic damping ratio, f_1 is the lower cut-off frequency, f_2 is the upper cut-off frequency and f_n is the resonance frequency of the power bandwidth curve which is shown in graph 17. The quality factor can also be calculated from the voltage decay curve or displacement decay curve for the system when subjected to an impulse excitation, according to equation [22]:

$$Q_p = \frac{\pi f_n \Delta t}{\ln\left(\frac{x_1}{x_2}\right)} = \frac{\pi f_n \Delta t}{\ln\left(\frac{V_1}{V_2}\right)}$$

In general, the unloaded quality factor of a miniature resonant generator is influenced by various factors. At its most general, it can be expressed as:

$$Q_p = \left(\frac{1}{Q_m} + \frac{1}{Q_t} + \frac{1}{Q_c} + \frac{1}{Q_{su}} + \frac{1}{Q_f} \right)^{-1} \quad (27)$$

where $1/Q_m$ is the dissipation arising from the material loss, $1/Q_t$ is the dissipation arising from the thermoelastic loss, $1/Q_c$ is the dissipation arising from the clamping loss, $1/Q_{su}$ is the dissipation arising from the surface loss, and $1/Q_f$ is the dissipation arising from the surrounding fluid. There have been considerable efforts to find analytical expressions for these various damping mechanisms, particularly for Silicon-based MEMS devices such as resonators. However further analysis of the parasitic damping factor is beyond in this chapter.

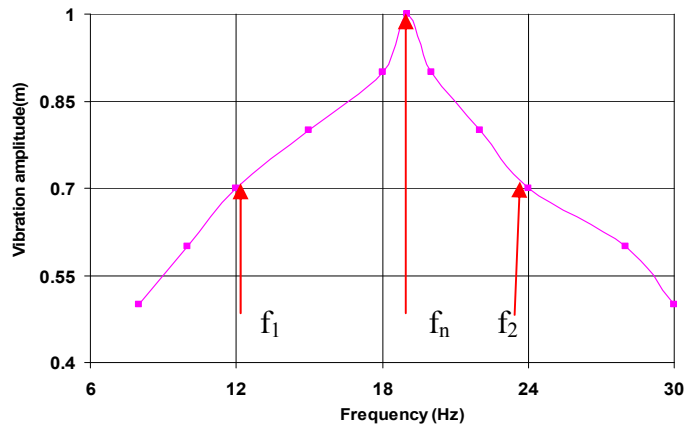


Fig. 17. Power bandwidth curve

1.7 Spring constant (k) of a cantilever beam

A cantilever is commonly defined as a straight beam, as shown in Figure 18 with a fixed support at one end only and loaded by one or more point loads or distributed loads acting perpendicular to the beam axis. The cantilever beam is widely used in structural elements and the equations that govern the behavior of the cantilever beam with a rectangular cross section are simpler than other beams. This section shows the equations that the maximum allowable vertical deflection, the natural frequency and spring constant due to the end loading of the cantilever.

The maximum allowable deflection the spring can tolerate is [27]:

$$y_{\max} = \frac{2L^2}{3Et} \sigma_{\max} \quad (28)$$

where σ_{\max} is the maximum stress, E is Young's modulus, t is the thickness of the cantilever, and L is the length of the cantilever.

The maximum stress can be defined as

$\sigma_{\max} = \frac{FLt}{2I}$ where F is the vertical applied force and $I = \frac{Wt^3}{12}$ is the moment of inertia of the beam.

The ratio between the force and the deflection is called the spring constant, k and is given by:

$$k = \frac{3EI}{L^3} \quad (29)$$

The total end mass of the beam is $m = 0.23M + m_1$

where m_1 is the added mass and M is the mass of cantilever.

The equation of motion for free undamped vibration is:

$m \frac{\partial^2 y}{\partial t^2} + ky = 0$, where, m is the total end mass of the beam. If $y = A \cos \omega_n t$ then the natural frequency would be,

$$f_n = \frac{1}{2\pi} \sqrt{\frac{k}{m}} \quad (30)$$

The next section presents the electrical circuit analogy of the electromagnetic vibrational generator.

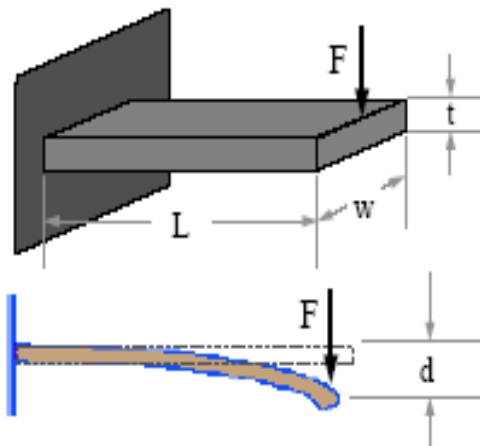


Fig. 18. Cantilever beam deflection

1.8 Equivalent electrical circuit of electromagnetic vibrational generator

The vibrational generator consists of mechanical and electrical components. The mechanical components can be easily represented by the equivalent electrical circuit model using any electrical spice simulation software in order to understand their interactions and behaviours. Two possible analogies either impedance analogy or mobility analogy is normally used in the transducer industry which compare mechanical to electrical systems. However it is good idea to use the analogy that allows for the most understanding and also it is easy to switch one analogy to other. Table 2 [29-30] shows the equivalent electrical circuit elements of the

mechanical components for the electromagnetic vibrational generator. Figure 19 shows the equivalent electrical circuit of the force driven electromagnetic linear or vibrational generator. When an external force (F) is applied to the generator housing or diaphragm the voltage will be generated at the coil terminal due to the relative displacement between magnet and coil. The moving mass, mechanical compliance, mechanical resistance, coil resistance, coil inductance, load resistance and the force factor of the alternator are M_m , $C_m = 1/k$, R_m , R_c , L_c , R_L and Bl respectively.

Mechanical elements	Equivalent Electrical elements	
	Impedance analogy	Mobility analogy
Force (F)	Voltage (E)	Current (I)
Velocity (U)	Current (I)	Voltage (E)
Mechanical resistance (R_m)	Resistance (R)	Conductance (G)
Mechanical mass (M)	Inductance (L)	Capacitance (C)
Mechanical compliance (C_m)	Capacitance (C)	Inductance (L)

Table 2. Electrical equivalent of the mechanical components.

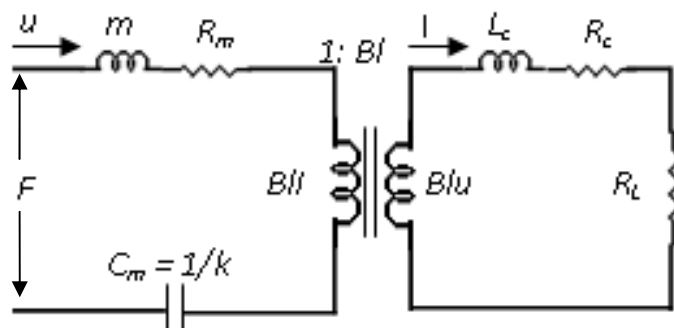


Fig. 19. Equivalent electrical circuit of the electromagnetic vibrational generator.

2. Verification of the model

In order to verify the model and the optimization theory several macro generators had been built and tested using a controllable shaker during Author's Ph.D study. Some of these works have already been highlighted in literatures [6]. It was important to vibrate the generator exactly at resonance in order to observe the electromagnetic damping effect for different load conditions. If the vibration frequency is far away from the system's resonant frequency, then the damping would not have any significant effect on displacement since the displacement is mainly controlled by the spring constant at off resonance. All the prototypes which have been built and tested consisted of four magnets (NdFeB35) with a wire-wound copper coil placed between the magnets as shown in Figure 20. The advantages of the four magnet generator structure have already been described in the previous section. Table 3 gives the coil and magnet parameters for macro generator A and B. The generators were vibrated using a sinusoidal acceleration with the frequency matched to the generator's mechanical resonant frequency.



Fig. 20. Generator A-showing four magnets attached to a copper beam and wire-wound coil.

Parameters	Generator -A	Generator-B
Moving mass (kg)	0.0428	0.025
Magnet size (mm)	15 x 15 x 5	10 x 10 x 3
Resonant frequency (Hz)	13.11	84
Acceleration (m/s ²)	0.78	7.8
Magnet and coil gap (mm)	1.25	1.5
Coil outer diameter (mm)	28.5	13.3
Coil inner diameter (mm)	5	2
Coil thickness (mm)	7.5	7
Coil turns	850	300
Coil resistance (ohm)	18	3.65

Table 3. Generator Parameters.

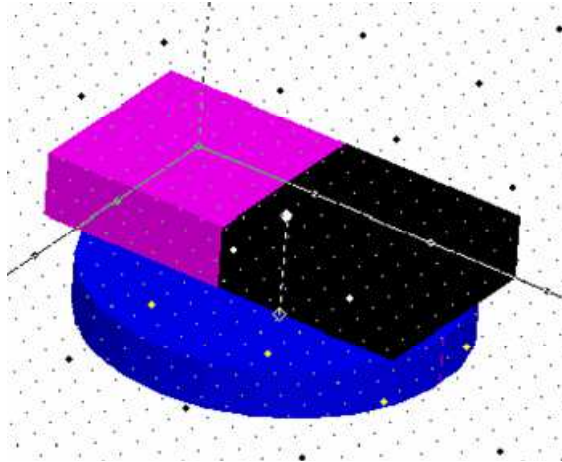
Measured and calculated results of the macro-generator A & B

The displacement and voltage were measured for various load resistances. The load power is calculated from the voltage and load resistance. The parasitic damping can be calculated using the no-load displacement equation:

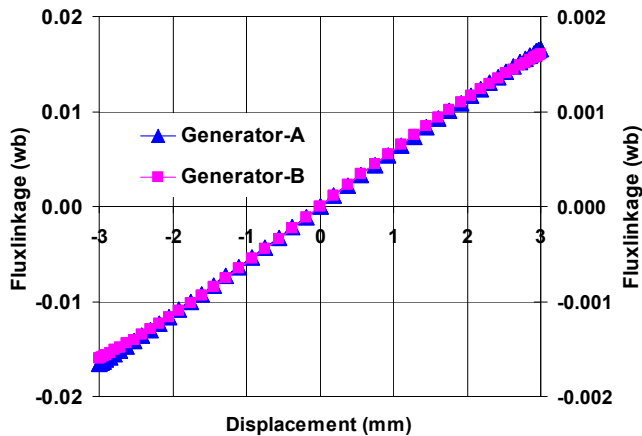
$$x_{no-load} = \frac{-F \cos \omega t}{D_p \omega}, \quad D_p = \frac{F_0}{x_{no-load} \omega}$$

The generators were also simulated using a 3-D finite element (FE) transient model with the measured displacement as input. Figure 21 shows the half model of the generator structure used in the FE model and the simulated flux linkage vs displacement of macro generator A

& B. The simulated flux linkage gradients ($\frac{d\phi}{dx}$) of the generator A and B are 0.00542 Wb/m and 0.0013 Wb/m respectively.



(a)



(b)

Fig. 21. Simulated Generator models used in (a) FE simulation and (b) the resulting flux linkage gradient vs displacement.

These values are used in the following equation to calculate the electromagnetic damping;

$$D_{em} = \frac{N^2 \left(\frac{d\phi}{dx} \right)^2}{R_c + R_l}$$

The parasitic and electromagnetic damping can then be used in the following equation to calculate the power:

$$P_{avg} = D_{em} \frac{F^2}{(D_p + D_{em})^2}$$

Figures 22 and 23 show the measured displacement and the measured and simulated load voltages for different load conditions for generator-A and generator B, respectively. The measured and simulated voltages agree quite closely. Figure 24 and 25 show the measured and calculated power, and the estimated parasitic and electromagnetic damping, for generators A and B, respectively.

The calculated open circuit quality factors $Q_{oc} = \frac{m\omega_n}{D_p}$ are

58.85 and 56.87 for generators A & B, respectively. The graph in Figure 22 shows that there is a significant change in displacement with the change in load, for generator A. However for generator B, the displacement does not vary with load. This is consistent with the fact that the electromagnetic damping is comparable to the parasitic damping for generator A, but the electromagnetic damping is much lower for generator B than the parasitic damping due to larger gap between magnet and coil, and smaller magnets used. This can be seen from figure 24 and 25. Furthermore, the graph in figure 24 shows that the power reaches a maximum for the value of load resistance at which electromagnetic damping and parasitic damping are equal. The optimum load resistance is 432Ω , which agrees well with the theoretical equation. For generator B, the electromagnetic damping is always much less than the parasitic damping and the power is maximized for a load resistance equal to the coil resistance. In figure 24 there is a small discrepancy between the measured and calculated power since the calculated power assumes a sinusoidal voltage but the measured voltage is not exactly sinusoidal.

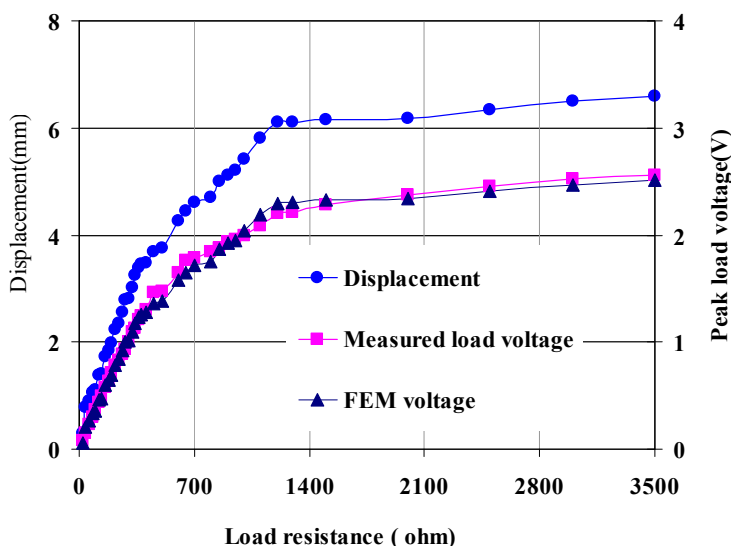


Fig. 22. Measured displacement and simulated and measured load voltage for generator A.

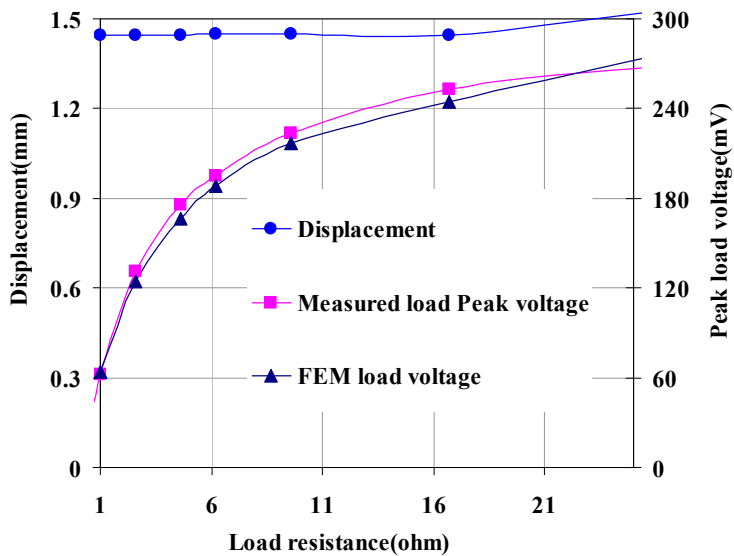


Fig. 23. Measured displacement and simulated and measured load voltage for generator B.

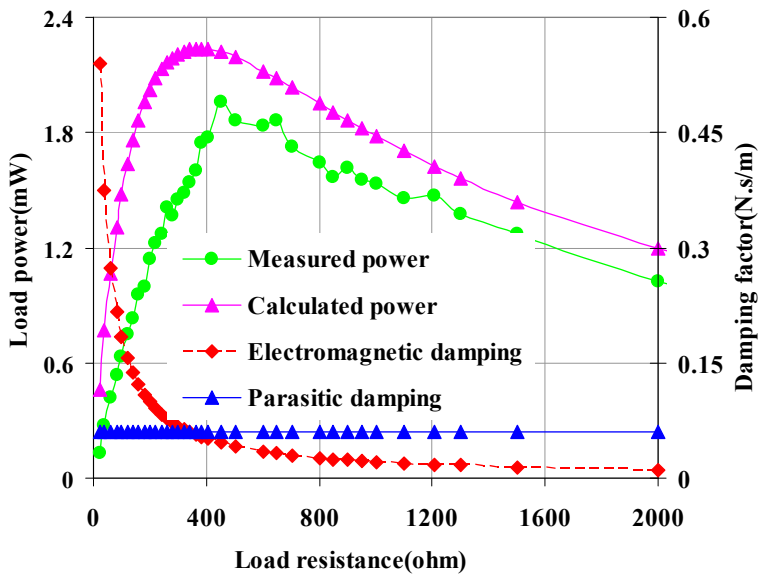


Fig. 24. Measured and calculated load power and estimated parasitic and electromagnetic damping for generator A.

In order to understand the parasitic damping effect and the optimum condition of the generator, more macro generators have been built and tested. Table 4 shows the generator

parameters of macro generators C, D and E. Generators C, D, and E were tested for different acceleration levels and the vibration frequency of the shaker was swept in order to determine the resonance frequency. In generators A and B, the parasitic damping factor and the open circuit quality factor were calculated from the measured no-load displacement. However, for generators C, D and E, the no-load and load voltages at the half power bandwidth frequency were measured in order to determine the open circuit and closed circuit quality factors and hence the damping. Figures 26, 27 and 28 show the no-load voltages for different acceleration levels of generators C, D, and E, respectively. It can be seen from these figures that as the acceleration level increases, the resonance frequency shifts to a lower frequency due to the spring softening characteristic of the spring constant [31]. This indicates that the displacement of the spring constant is approaching the non-linear region. However, the resonance frequency could also shift to a higher frequency with increased acceleration level which is normally known as a spring hardening characteristic.

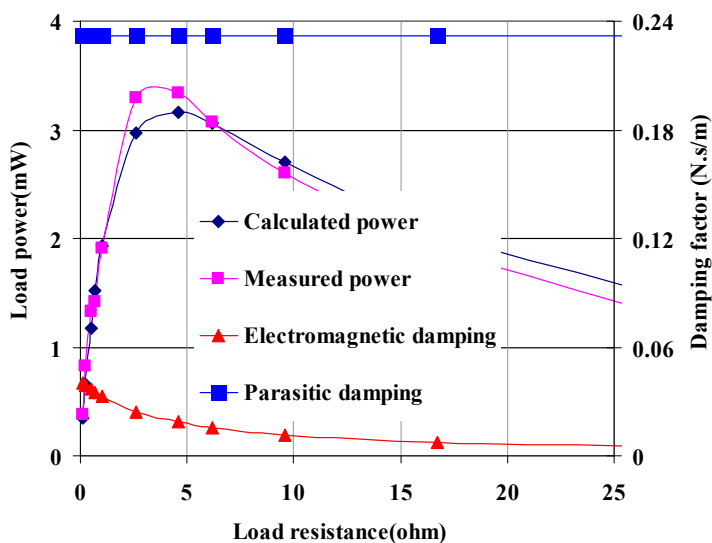


Fig. 25. Measured and calculated load power and estimated parasitic and electromagnetic damping for generator -B.

Parameters	Generator -C	Generator-D	Generator-E
Moving mass (kg)	0.019579	0.05116	0.05116
Magnet size (mm)	10 x 10 x 3	15 x 15 x 5	15 x 15 x 5
Magnet and coil gap (mm)	3.75	3.75	3.25
Coil outer diameter (mm)	19	19	28.5
Coil inner diameter (mm)	1	1	5
Coil thickness (mm)	6.5	6.5	7.5
Coil turns	1100	1100	850
Coil resistance (ohm)	46	46	18

Table 4. Generator parameters

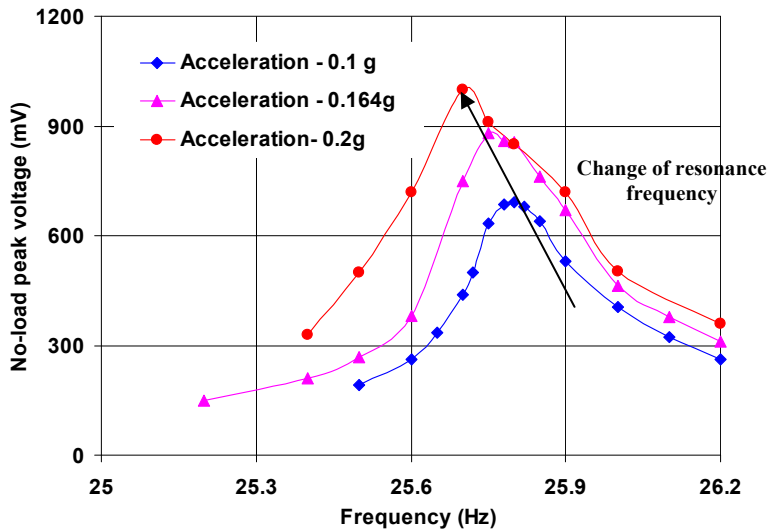


Fig. 26. No-load voltage vs frequency of generator - C.

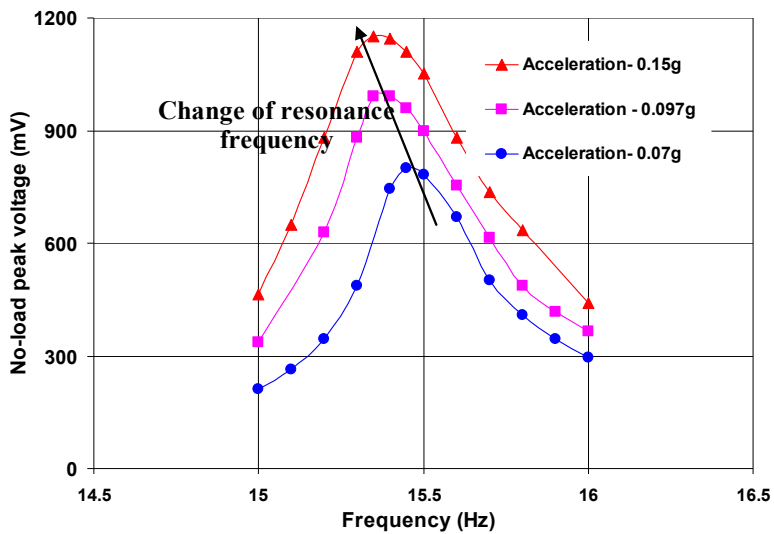


Fig. 27. No-load voltage vs frequency for generator-D.

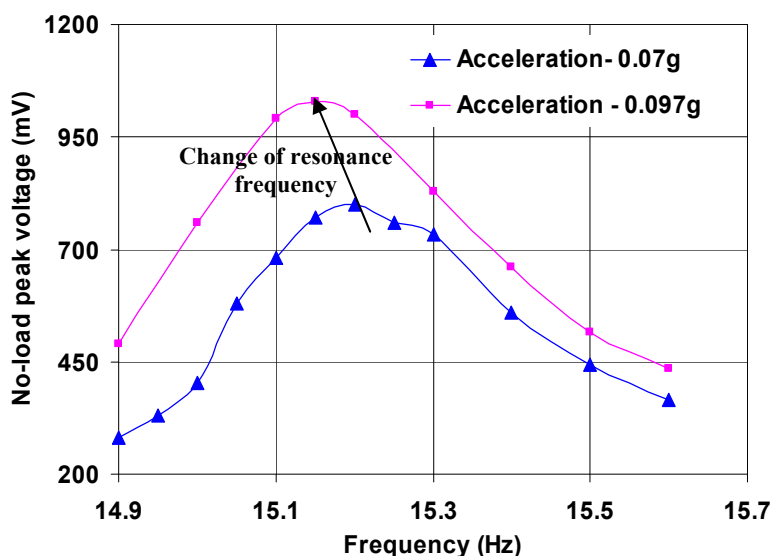


Fig. 28. No-load voltage vs frequency for generator-E.

This non-linear mass, damper and spring vibration can be defined by the standard Duffing oscillator model [31] using the following equation;

$$m \frac{d^2 x}{dt^2} + D \frac{dx}{dt} + kx + k_3 x^3 = F \sin \omega t \quad (31)$$

It can be seen in the above equation that a cubic nonlinear stiffness term ($k_3 x^3$) has been added to the linear mass, damper, and spring equation. If the non-linear stiffness constant (k_3) is greater than zero then the model would represent a hardening spring constant. In this case, the resonance frequency would be shifted to the right (increase) from the linear resonance frequency with increased vibrational force, as shown in Figure 29 (a). If k_3 is less than zero, then the model would represent a softening spring constant. In this case, the linear resonance frequency would be shifted to the left (decrease) from the linear resonance frequency with increased vibrational force, as shown in Figure 29 (b).

Table 5 shows the calculated open circuit quality factor, parasitic damping factor, optimum load resistance, measured generated electrical power and load power on the optimum load resistance of each generator for different accelerations. The open circuit quality factor and the parasitic damping were calculated using the following formulas;

$$Q_{oc} = \frac{f_n}{f_2 - f_1}, \quad D_p = \frac{m \omega_n}{Q_{oc}}$$

The displacements of the generators for each load were calculated according to the equation;

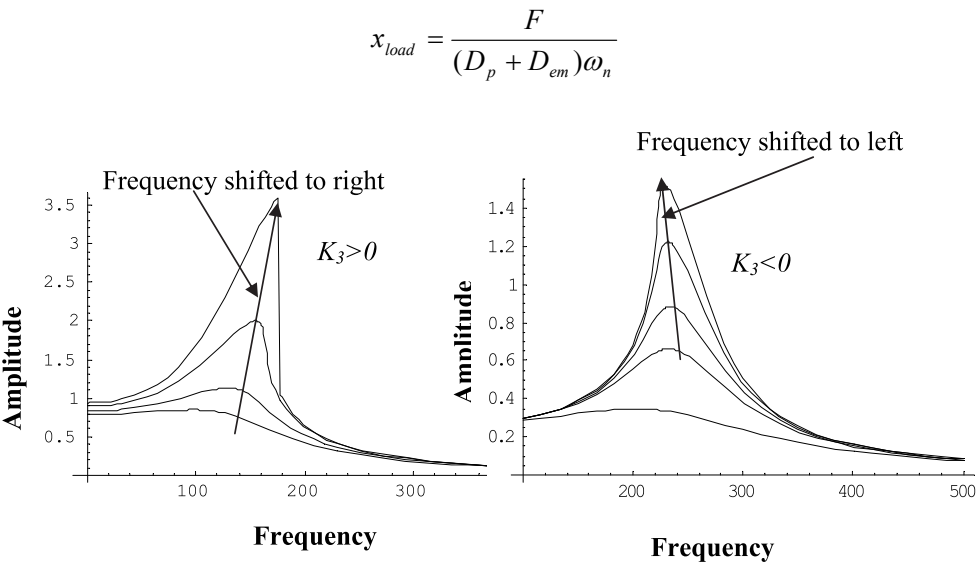


Fig. 29. Amplitude response of (a) non linear hardening spring constant (b) non linear softening spring constant.

Generator -C								
Accelerati on (g)	Q _{oc}	X _{no- load(mm)}	D _p (N.s/m)	R _c (Ω)	R _{lopt} (Ω)	D _{em} @ R _{lopt}	Generated electrical power (mW)	Max. load power (mW)
0.10	86	3.21	0.036	46	100	0.012	0.95	0.65
0.16	67	4.16	0.046	46	75	0.019	1.90	0.95
0.20	59	4.49	0.052	46	75	0.019	2.28	1.14
Generator -D								
0.07	40	2.99	0.122	46	75	0.065	1.34	0.83
0.10	36	3.76	0.133	46	75	0.065	2.23	1.38
0.15	29	4.69	0.166	46	75	0.065	3.20	1.98
Generator -E								
0.07	38	2.96	0.13	18	75	0.105	1.53	1.24
0.097	35	4.27	0.12	18	100	0.105	3.00	2.20

Table 5. Calculated parasitic damping and measured power for optimum load resistance.

The generators were also simulated using a FE transient model in order to verify the measured results with the simulated value. For example Figures 30 and 31 show the measured and simulated voltages and power respectively of the generator-C for 0.1g acceleration level. The graphs show that the measured voltages and power agree well with the FE simulation voltages. Table 5 shows that the maximum power of generator-E are transferred to the load when the parasitic damping equals the electromagnetic damping; this agrees well with the theoretical model. Generator-E delivers a maximum 81% of the generated electrical power to the load. In generator-C and D, significant electromagnetic

damping is present but it is still not high enough to match the parasitic damping. The optimum load resistances for all of these generators at the maximum load power agree well with the prediction of equation (24).

It can also be seen from Table 5 that the parasitic damping is not constant for different acceleration levels. It appears that parasitic damping increases with increasing displacement. This parasitic damping depends on material properties, acceleration, size and shape of the generator structure, frequency and the vibration amplitude, as has already been explained earlier. As a consequence of this, the optimum load R_{lopt} can be different for different acceleration levels, as in the case of Generator -C.

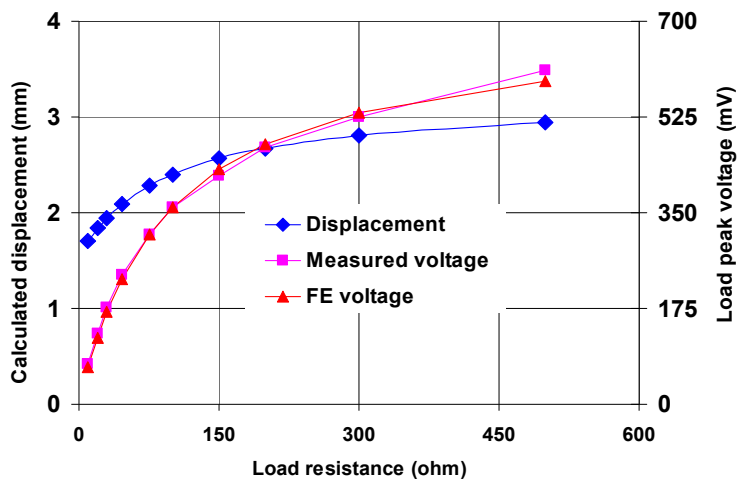


Fig. 30. Displacement and Measured and FE load voltages of generator-C for 0.1g acceleration.

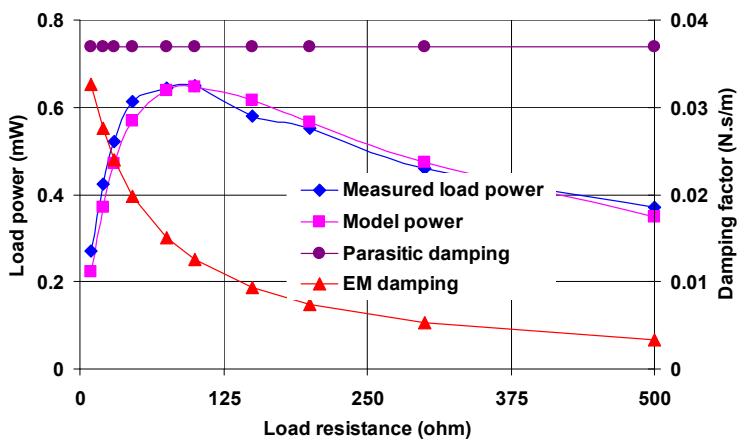


Fig. 31. Measured and calculated load power and estimated parasitic and electromagnetic damping of generator-C for 0.1g acceleration.

The power graphs for different acceleration levels of generator C & D are plotted in Figure 32 to establish the relation between the generated electrical power and the applied acceleration. According to linear theory, the generated electrical power should have a square law relation with the acceleration and an inverse square relation with total damping

factor ($P_{avg} = D_{em} \frac{(ma)^2}{2(D_p + D_{em})^2}$). It can be seen from this graph that in practice the generated

electrical power did not vary squarely with the variation of the acceleration. This is again due to the variation of parasitic damping factor, i.e as a is increased, D_p also increases and thus in practice the power has closer to a linear variation with acceleration. The next section will provide the available vibrational sources which are present in the environment since ultimate goal for energy harvester is to generate useful electrical energy from the environment.

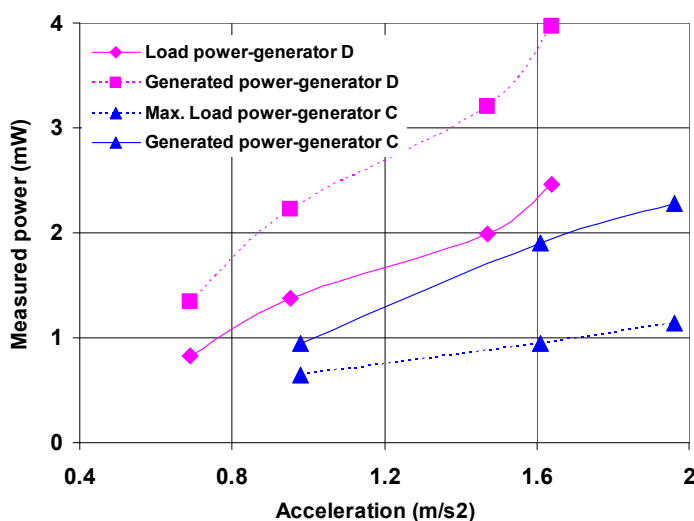


Fig. 32. Power vs acceleration

2.1 Vibrational sources

It is necessary to understand the acceleration and frequency level of different vibration sources. Since the ultimate goals of the energy harvesting device is to generate electricity from ambient sources. An overview of a variety of commonly available vibrations has already been published in several literatures [2,9]. Most of them are classified as low level vibrations which are characterised by higher frequencies and smaller amplitudes, such as industrial, automotive and structural applications and some of them are characterised by low frequency and high amplitude, such as human motions.

2.1.1 Human motion

Human motion occurs during physical activities such as walking, jogging and running. The electromagnetic vibrational generator could be mounted or attached at different

locations on the human body, wired into clothes, foot-wear, a belt bag, rucksack, etc to power electronic devices using these activities. However, the amplitude, frequency, and nature of the vibration can be quite different at different locations on the human body and the acceleration would be quite high and frequencies are very low in these circumstances. For example, the acceleration level in different locations on the human body is shown in Figure 33 during walking, jogging and running on a treadmill (measured for VIBES project [31-33]). Table 6 summarises a few examples of the measured acceleration levels during walking when the accelerometer was tightly fastened on the ankle, wrist and chest. It can be seen that the maximum vertical acceleration level can be achieved at the ankle with 108 m/s^2 compared to 25 m/s^2 on the wrist and 6.6 m/s^2 on the head (front). The maximum vertical acceleration levels during walking and slow running condition were 4.9 m/s^2 ($0.5g$) and 9.81 m/s^2 ($1g$) when the accelerometer was placed in rucksack bag, as shown in Figure 34. It can be seen from this measurement that vibration is irregular and consists of high amplitude impulse like excitation rather than sinusoidal excitation and the frequency is less than 3 Hz . A resonant generator may not be the most suitable for human motion due to low frequency, high amplitude and irregular nature of human movement. Since the vibration signal in human motion tends to be non-sinusoidal random vibration, a suitable generator structure is necessary which can vibrate easily at off resonance conditions.

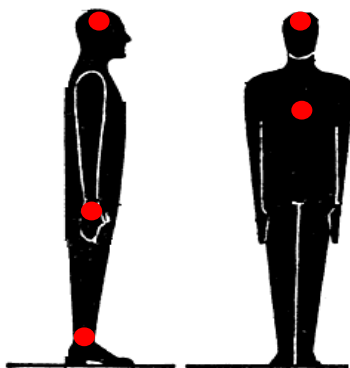


Fig. 33. Accelerometer locations on the human body.

Location	Maximum acceleration (m/s^2)
Ankle	108
Wrist	25
Chest	16
Head (front)	6.6

Table 6. Summary of acceleration levels on the human body.

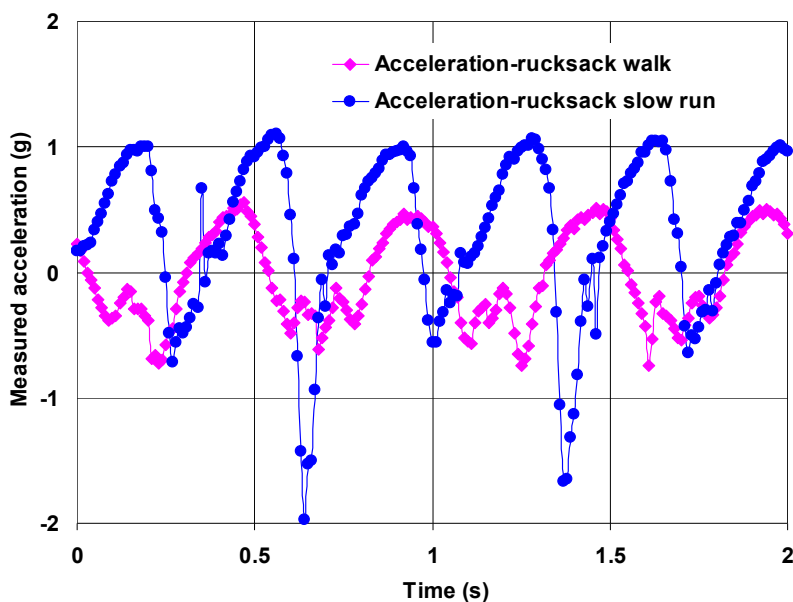


Fig. 34. Measured acceleration inside rucksack bag during walking and slow running.

2.1.2 Home appliance, machinery and automotive vibration

Vibrations from automotive applications give rise to frequencies of tens of Hz to several hundred Hz but with smaller accelerations. The vibrations generated from home appliances such as clothes, dryers, small microwave ovens and blender casings [9],[31],[32] are similar. Vibrations from rotating machines, such as pumps and fans, can include quite high frequency components, but are in general limited to relatively small accelerations. The rotational speed of these machines is constant and generates several harmonic frequency vibrations which consist of multiples of the fundamental frequency corresponding to the rotational speed. The vibration spectrum of an industrial fan (nominal speed 1500 rpm- 25 Hz), pump (nominal speed 3000 rpm-50 Hz) and air compressor unit were measured in different positions of the machines for the VIBES project [5], [33]. Figure 35, 36 and 37 show the vibration spectrum of an industrial fan and top and bottom of an air compressor unit at different positions. It can be seen from the graphs that the vibration signal is quite low amplitude with multiple vibration peak frequencies. It can be seen that all these have a peak at or near 50 Hz, 100, 150 or 250 Hz. A resonant generator structure is essential for this application in order to achieve a reasonable displacement from this very low amplitude vibration. Table 7 shows the available acceleration and frequency level of the different home appliance, machinery and automotive sources. In the following section, we present such a generator and measure the power generated from human motion when the generator is placed in a rucksack. The generator makes use of a “magnetic spring” as opposed to a mechanical spring, which could give advantages such as ease of construction, ease of tenability, and lower sensitivity to fatigue.

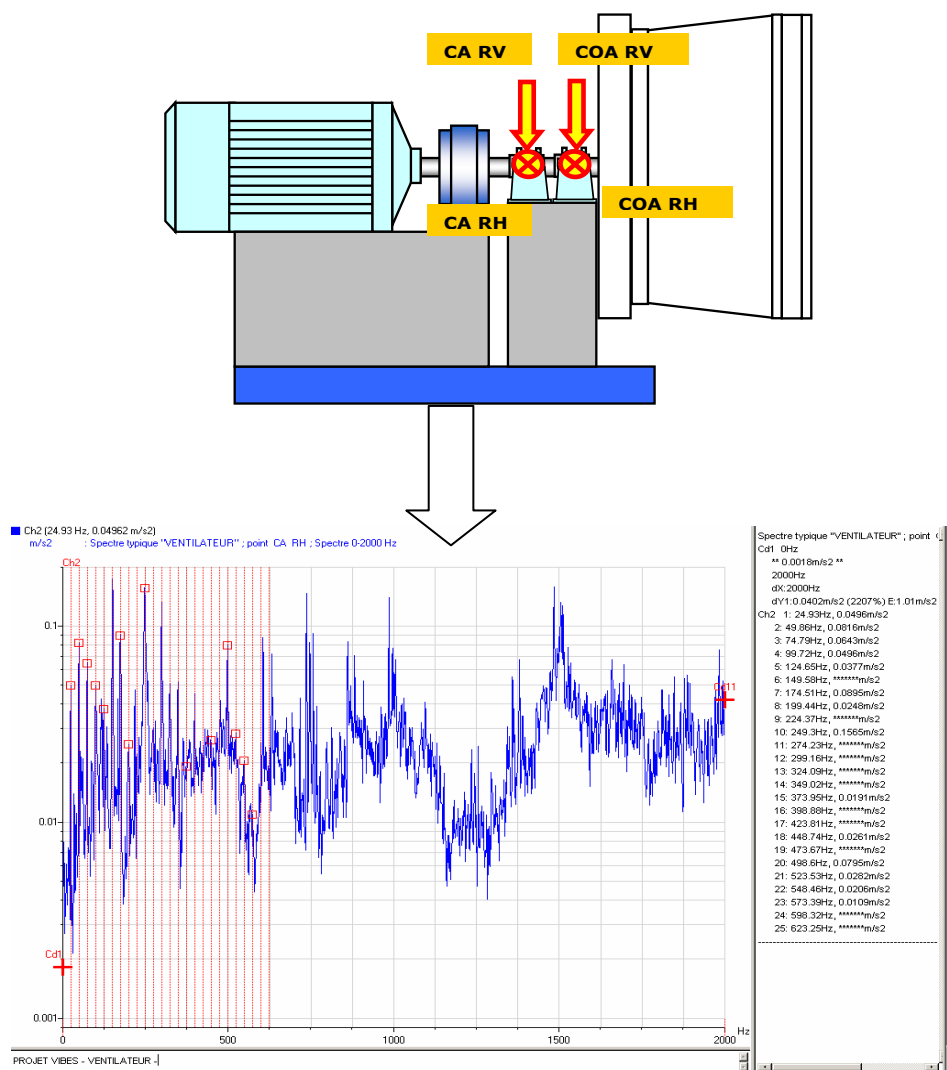


Fig. 35. Measured vibration spectrum of the industrial fan from [33].

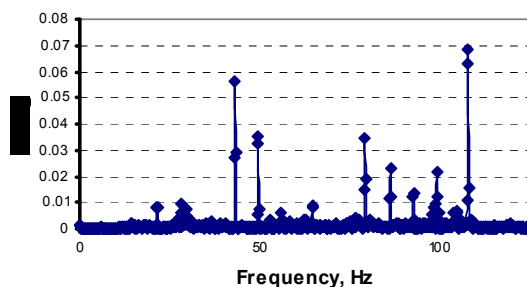


Fig. 36. Measured vibration spectrum on top of the air compressor unit [5]

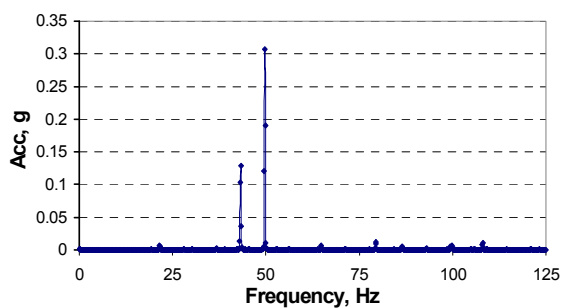


Fig. 37. Measured vibration spectrum at the bottom of an air compressor unit [5]

Vibration source	Fundamental frequency (Hz)	Acceleration (m/s ²)
Car engine compartment	200	12
Base of 3-axis machine tool	70	10
Blender casing	121	6.4
Clothes dryer	121	3.5
Car instrument panel	13	3
Door frame just after door closes	125	3
Small microwave oven	121	2.5
HVAC vents in office building	60	0.2-1.5
Windows next to a busy road	100	0.7
CD on notebook computer	75	0.6
Second story floor of busy office	100	0.2
Vehicle -C (high way)	15.13	1.987
Vehicle -C (mountain)	36.88	0.0175
Vehicle-C (city)	52.87	0.0189
Industrial fan	25	0.7
Pump	50	1.4

Table 7. Home appliance, machinery and automotive vibration

2.2 Magnetic spring generator and its applications

An electromagnetic vibrational generator could be used to power electronic devices using human body activity would be considerable interest. In such an application, For example, a displacement of $x = \frac{ma}{D\omega_n} = 9.75 \text{ mm}$ could be achieved for a mass of m of 10 mg, a of 4.905 m/s², D of 0.4 N.s/m at f_n equal to 2 Hz.

In this case, the generated electrical power, $P = D_{em} \frac{(ma)^2}{2(D_p + D_{em})^2} = 1.5 \text{ mW}$ assuming EM damping can be made equal to parasitic damping.

It can be seen from this simple calculation that at least several cm size generators are required. In particular, a cantilever resonant generator structure would not be realistic for such a low frequency application. If we consider a 3 mm width and 50 μm thick Si or Cu cantilever beam, the length of the cantilever for a 10 mg mass and 2 Hz frequency would be:

$$k = \frac{3EI}{L^3} = m\omega_n^2 \Rightarrow L = 290 \text{ mm}$$

In order to achieve a 10 Hz frequency, a Si cantilever would have to be a 100 mm long. We present such a generator and measure the power generated from human motion when the generator is placed in a rucksack. The generator makes use of a “magnetic spring” as opposed to a mechanical spring, which could give advantages such as ease of construction, ease of tenability, and lower sensitivity to fatigue. Some of these results have already been highlighted in literature [4].

Figure 38 shows different possible configurations for the magnetic spring generator structure. The basic idea is that axially magnetized permanent magnets are placed vertically inside a tube so that facing surfaces have the same polarization. Thus, the magnets repel one another. Two magnets are fixed at both ends of the generator tube housing. A middle magnet or magnets is free to move but is suspended between both fixed end magnets in the generator housing due to the repulsive force. A coil is wrapped around the outside of the tube. When the tube is vibrated, the middle magnet vibrates up and down, and a voltage is induced in the coil. This structure can be built easily since the generator simply consists of magnets and a coil without the need for any mechanical beam. Essentially the suspended moving magnet acts like a magnetic spring constant. This construction is similar to the inductively powered torch [34], except with the addition of a magnetic spring. We know that the generation of voltage is the product of flux linkage gradient and velocity. In order to increase the flux-linkage, the single moving magnet can be replaced by two magnets separated by a soft magnetic “pole” piece, where the magnets and pole piece are glued together so that they move as a single object as shown in Figure 38 (b). The variation of flux-linkage between the single moving magnet and double moving magnets plus pole structure generator will be shown in the next section.

In order to increase the displacement, instead of using two fixed magnets, the generator could be built using only one fixed end magnet and a single moving object, as shown in Figure 38 (c). In this case, the resonant frequency would be lower and the displacement of

the moving magnet would be higher compared to both fixed end magnets. The benefit of this concept in a human motion powered generator can be explained by considering the response of a spring damper system to an impulse excitation :

$$\begin{aligned} X(t) &= F_0 / k, \text{ for } [0 < t < t_0] \\ &= \exp(-\xi\omega_n t) X \sin(\omega_d t + \phi) \text{ for } [t > t_0] \end{aligned} \quad (32)$$

When the top magnet is removed from the generator, the effective spring constant is decreased and hence the resonant frequency is decreased. Thus according to equation (32), the initial displacement will be greater and the decay rate will be slower, which would result in increased voltage and larger average power. This concept will be verified with the measured results of the real prototype which has been built and tested.

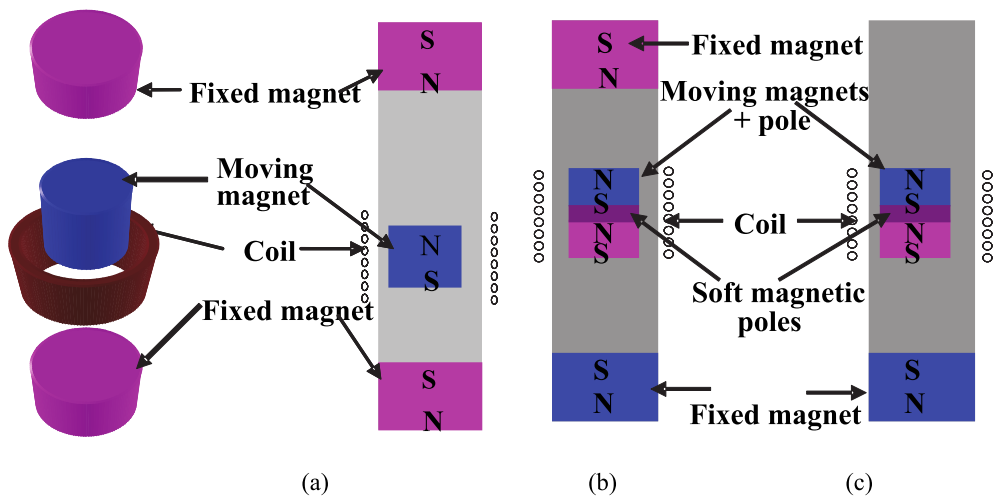


Fig. 38. Magnetic spring generator structure: (a) Single moving magnet (b) Single moving magnet replaced by two magnets + pole (c) One fixed magnet.

2.3 Analysis of generator structure

The generator structure has been modeled using Finite Element Analysis (FEA) in order to understand the spring forces which exist between the fixed and moving magnets and to understand the flux linkage with the coil. Figures 39 (a) and (b) show the results of an axis-symmetric finite element simulation of the corresponding generator structure of Figure 32 (a) and (b), respectively, showing magnetic field lines. In Figure 39 (a), a 15 x 19 mm single moving magnet is used. In Figure 39 (b), 15 x 8 mm double moving magnets and a 15 x 3 mm ferrite core are used. The overall generator dimensions are given in the next section. Figure 40 shows a plot of the radial component of the B field along a line extending from the top to the bottom of the generator for both of the generator structures. It can be seen from these field plots that the peak flux density for the double moving magnets with the pole piece is almost twice as high as for the single moving magnet generator structure. Thus, the flux gradient is higher, which translates into higher voltages and higher electromagnetic damping.

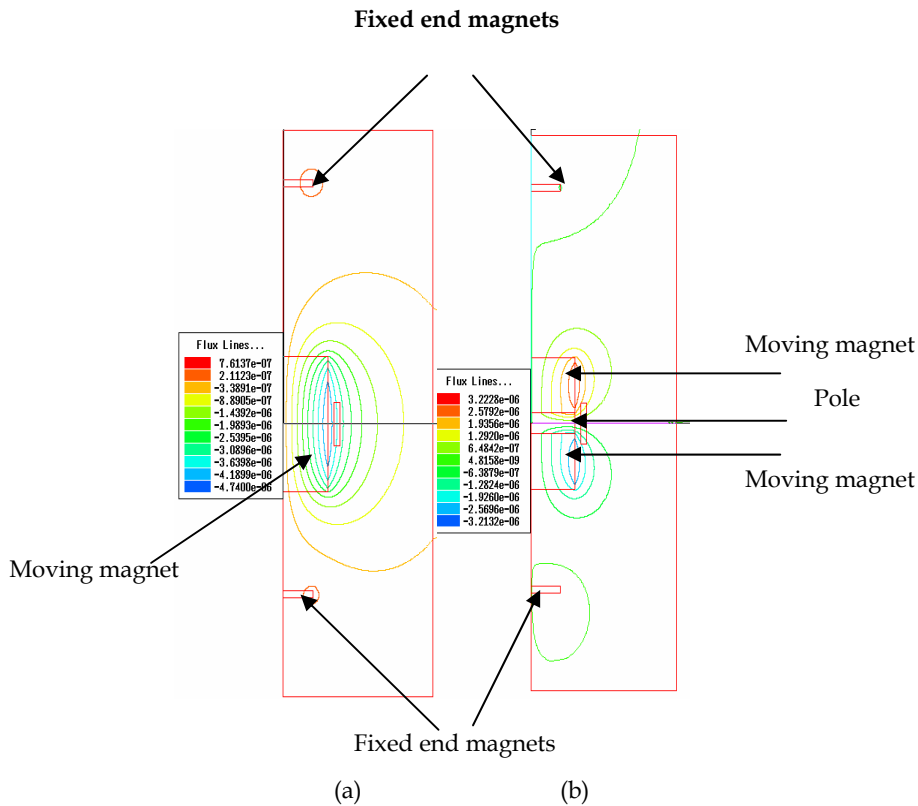


Fig. 39. Finite element simulation, showing flux lines for a) single moving magnet b) double moving magnets plus pole generator structure.

It is also of interest to investigate the dependence of the force between the magnets poles, which can be expressed analytically [35] as:

$$F_m = \frac{\mu_0 Q_{m1} Q_{m2}}{4\pi r^2} \quad (33)$$

where $Q_m = H_c A$, H_c is the coercive force and A is the pole surface area, r is the distance between the poles. The spring constant, k , over small displacements, x , can be calculated from the linear approximation of the balanced forces equation:

$$kx = F \quad (34)$$

where the total force, F , acting on the centre magnet is given by $F = F_{m1} - F_{m2}$, F_{m1} and F_{m2} are the repulsive force magnitude on the middle magnet due to the top and bottom magnets respectively. The electromagnetic force and spring constant can be calculated from a FE transient simulation using the force vs displacement graph for the double moving magnets

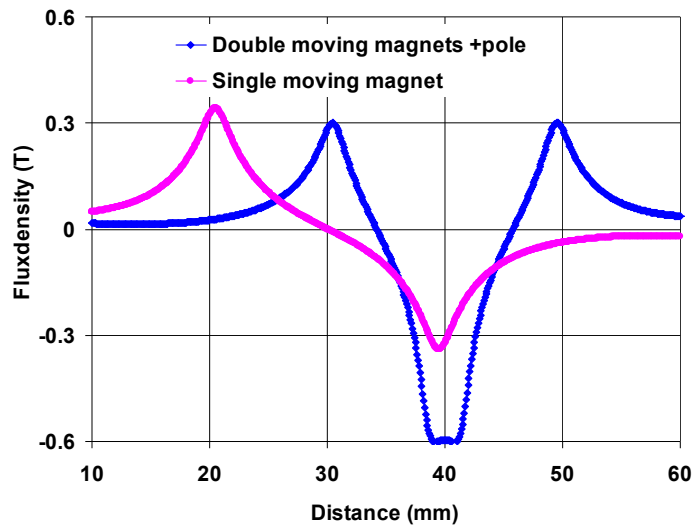


Fig. 40. Plot of radial component of flux density along a coil surface line extending from the top of the magnet tube to the bottom.

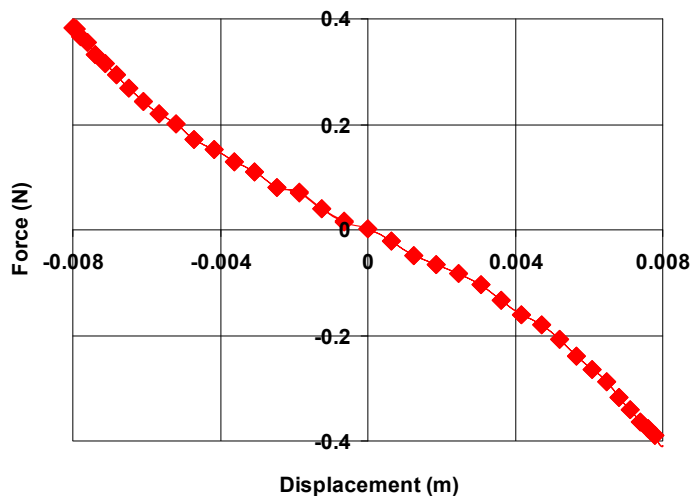


Fig. 41. Electromagnetic force vs displacement of the double moving magnets + pole generator.

plus pole structure generator which is shown in Figure 41. The resting position of the moving magnets is 4 mm away from the middle position due to the gravitational force. It can be seen from this graph that the electromagnetic force on the moving magnets is almost linear with displacement. The spring constant between the 4 mm to 8 mm region can be linearised and estimated from the graph as 61.5 N/m. In order to calculate the voltage and

the electromagnetic damping factor, the flux linkage gradient is also necessary. This flux linkage gradient can be calculated from the simulated displacement and flux linkage graph as shown in Figure 42. The gradient from + 4 mm to -4 mm is 23 Wb/m. The coil can always be positioned to take advantage of this flux gradient.

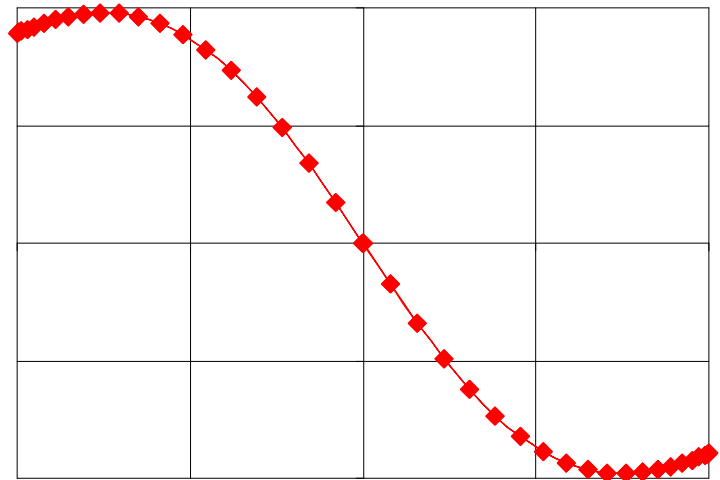


Fig. 42. FE simulated flux linkage gradient for the double moving magnets + pole generator.

2.4 Generator prototype and test results

The generator prototype consists of two opposite polarity circular magnets tightly glued to a 3 mm thick steel pole piece. This combination was inserted into a hollow Teflon tube so that it can move freely. After inserting, the two opposite polarity magnets were fixed on the both ends of the Teflon tube and 40 μ m copper wire with 1000 turns coil was wrapped around the tube, offset by -4 mm away from the centre of the tube. Figure 43 shows the prototype which has been built, pictured beside a standard AA size battery. The complete dimensions and parameters of the generator are given in Table 8.

Parameters	Dimension
Tube (mm)	17 X 55
Middle magnets (mm)	15 X 8
End magnets (mm)	10 X 1
Moving mass (kg)	0.027
Coil outer diameter (mm)	18
Coil inner diameter (mm)	17
Coil thickness (mm)	6
Coil resistance (ohm)	800

Table 8. Generator parameters



Fig. 43. Tube generator -1

2.4.1 Measured results for sinusoidal acceleration

For the first tests, the generator mounted it vertically on a force controlled electromagnetic shaker. The vibration frequency of the shaker was swept in order to determine the resonant frequency of the moving magnet combination. Any system always generates maximum vibration at the resonance condition and resonance occurs when the system natural frequency matches with the vibration frequency.

Figure 44 shows the no-load voltage vs frequency curve for 0.38259 m/s^2 acceleration level. It can be seen that the resonant frequency of the generator is at approximately 8 Hz. The theoretical resonant frequency, calculated from $\omega_n = \sqrt{k/m}$, where the spring constant, k , was estimated from the previous simulation, is 7.6 Hz. The measured open circuit quality factor of the generator can be estimated from the frequency response to be 18. The maximum load power measured was $14.55 \mu\text{W}$ using $7.3 \text{ k}\Omega$ load resistance where the electromagnetic damping and parasitic damping are equal. However, the aim of this generator is not to excite it with sinusoidal excitation but to excite from human movement. In the next section, we present the measured and calculated results for the prototype with human body movement.

2.4.2 Measured results of the generator for human body vibration

The generator was placed inside a rucksack and the voltage and power outputs were measured during walking and slow running conditions. An ADXL321 bi-axial accelerometer was mounted on the generator body and connected to an XR440 pocket data logger. The pocket data logger was used to measure the generator load voltage and the acceleration levels experienced by the generator.

The measured acceleration for 2 seconds data during walking and slow running conditions has already been discussed in the application section. The data shows peak acceleration levels of approximately $0.5g$ with a frequency of 2 Hz for walking and peak acceleration levels of approximately $1g$ with a frequency of approximately 2.75 Hz for slow running.

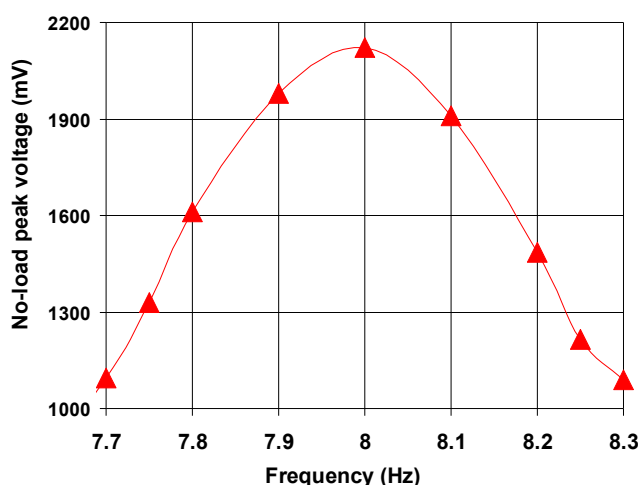


Fig. 44. Measured no-load peak voltage for half power bandwidth frequency.

Figure 45 shows the measured generated voltage graph during the walking and slow running conditions. It can be seen that the generated voltage for the slow running case is more than two times higher than for the walking case. The average load powers of the generator were measured to be 0.30 mW for walking and 1.86 mW for slow running when the coil resistance and load resistance are matched.

A second version of this generator, without a top fixed magnet, was also tested in order to compare the difference in the system frequencies, generated voltages and power levels. Figure 46 shows the measured generated voltage graph during the walking and slow running conditions. The average measured maximum load powers of the generator without top fixed magnets were 0.95 mW and 2.46 mW during the walking and slow running conditions respectively. Comparing this to the power levels obtained from the generator with both fixed magnets, it can be seen that the power level is increased three times during walking but the power level during the slow running condition is increased by only 32 %. During the slow running condition, the magnet displacement is large and it moves outside the coil where it does not generate any more voltage or power. In this case, the dimensions of the coil should be optimized for the expected displacement. In order to verify the generator voltage obtained from a single shock, the impulse responses of both generators were captured in an oscilloscope and are shown in Figure 47. It can be seen that the natural frequency and decay rate are higher in the case of the top and bottom fixed end magnet generator than the generator without top fixed magnet generator. Due to the lower spring constant the generator without the top end magnet gives a higher displacement of the moving magnet as well as a higher voltage. This is consistent with equation (32) discussed earlier.

Ultimately, the electrical energy generated will have to be stored in either a rechargeable battery or a capacitor. Thus it is of interest to investigate how much energy the generator can store over a certain period of time. The generator was placed inside a rucksack and the

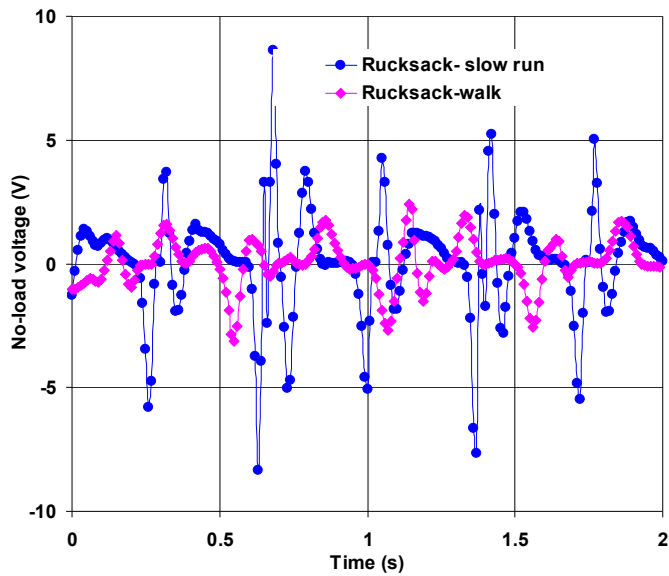


Fig. 45. Measured no-load voltage during walking and slow running when the generator was placed inside rucksack bag.

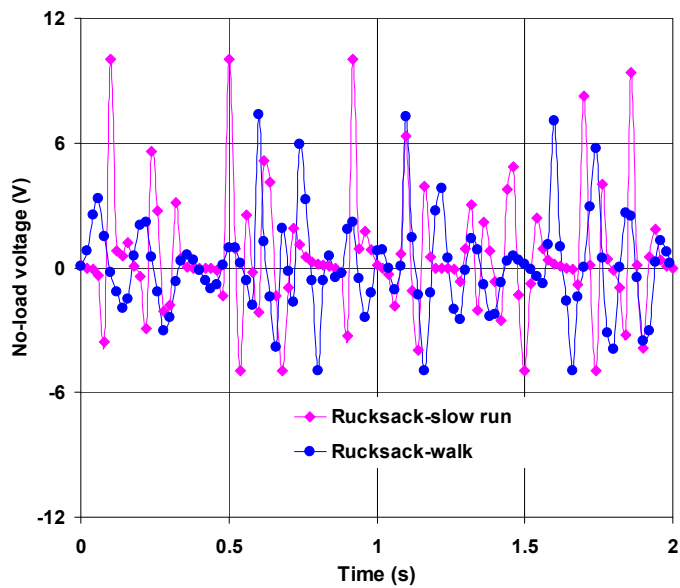


Fig. 46. Measured no-load voltage during walking and slow running for generator with only one fixed magnet.

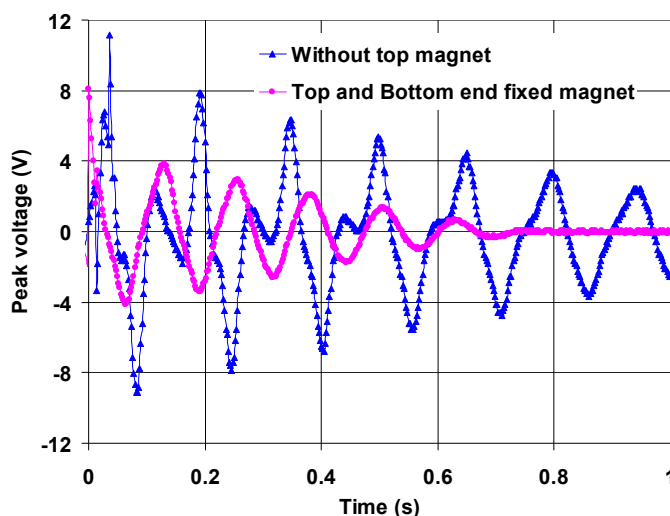


Fig. 47. Impulse responses of generators with both fixed end magnets and only one fixed end magnet.

output was connected to a rechargeable Li-MnO₂ Varta coin cell (Maxwell-ML1220) through a simple diode capacitor rectifier circuit. The battery was initially discharged to a voltage of 1.09 V. After 1 hour walking, the battery voltage had increased from 1.09 V to 1.27 V. In order to calculate the energy transfer during this time, the discharged characteristic curve of the battery was measured with a 5.5 k Ω load using the pocket logger. The measured results show that 3.54 joules of energy is transferred to the battery from the generator. This energy level is consistent with the powering of low power sensor modules without a battery. For example, the power consumption of a wearable autonomous Microsystem which consists of a light sensor, a microphone, accelerometer, microprocessor and a RF transceiver is 700 μ W which is equivalent to 2.5 joules [36]. The cantilever prototypes which have been built and tested were not optimised and were not built for a specific application. Since the eventual goal would be the integration of the generator into autonomous sensors modules, a miniature generator is essential. In the following section, we will present a prototype of an optimised micro generator and its applications.

2.5 Cantilever micro generator and its applications

The theoretical model of the electromagnetic vibrational generator had been discussed and successfully verified with the different macro scale cantilever prototype generators which have been built and tested. Magnetic spring generator had also been tested using real human body applications. However all the prototypes were not optimized and it is essential to optimize the generator for specific application in order to reduce the cost and size. Few optimized micro generators had been built and tested by the University of Southampton for air compressor application [5]. The theoretical analysis and the verification of the measured results have been done as part of Author's Ph.D work for the VIBES project. The details optimization concepts of those micro generators were explained in the literature [5].

However in this section we will highlight some parts of those results. Figure 48 shows the VIBES optimized microgenerator associated with the electronics.

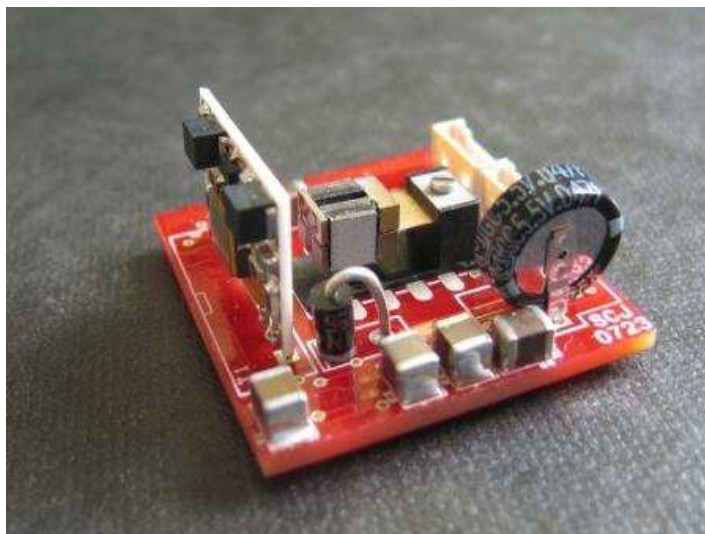


Fig. 48. VIBES generator associated with electronics powering the accelerometer.

The generator generates maximum power and delivers maximum power to the load when the electromagnetic damping factor equals the parasitic damping factor. Since the parasitic damping is fixed for the particular generator within linear movement, the electromagnetic damping factor can be increased by using the optimum magnet size for a particular coil, using more coil turns, and keeping the gap between the magnet and coil as low as possible. It can be seen from the following equation of electromagnetic damping that it has a square law relation with the number of coil turns and the flux linkage gradient:

$$D_{em} = \frac{N^2 \left(\frac{d\phi}{dx} \right)^2}{R_c + R_l}$$

In order to achieve the maximum flux linkage gradient, the optimum magnet for a particular coil and the lowest possible gap between magnet and coil is necessary. Three optimised micro generators with 600-, 1200- and 2300 turns coil with identical mechanical dimension have been built and tested for different acceleration levels for target application of the air compressor unit. These three generators differ only in the number of turns in the coil. Each coil was mounted on the same generator base and the same beam was assembled on each base. The 70 μm thick single crystal silicon cantilever beam which was used in the initial micro generator which was found to be too brittle to handle during assembly. The resonance frequency of the 70 μm silicon beam was 91 Hz. The targeted application is an air compressor unit which has a resonance frequency in the 50-60 Hz range. In order to reduce the resonance from 91 Hz to 60 Hz, either we have to increase the beam length or decrease

the beam thickness. Instead of using a 70 μm silicon beam, a 50 μm BeCu beam was used for the optimized micro generators. BeCu has better fatigue characteristics and less brittle behaviour [5] compared to Si but both have the same Young's modulus properties. The calculated resonance frequency of the 50 μm beam is 55 Hz, which is very close to the target application frequency. This frequency can be adjusted to the required 50 Hz or 60 Hz frequency during assembly. Table 9 shows the three principle parameters of the coil.

Wire diameter, λ (μm)	No. of turns	R_{coil} (Ω)	Fill factor
25	600	100	0.67
16	1200	400	0.63
12	2300	1500	0.53

Table 9. Coil parameters.

In order to analyse the measured results with the linear modelling approach, initially the micro generator with the 600 turn coil has been tested for different acceleration levels within the linear region of the spring constant. Figure 49 shows the measured and calculated power with an optimum load resistance of 200 Ω up to 30 mg acceleration. The generated mechanical, generated electrical and the load power are calculated using the following equations:

$$P_{\text{mech}} = \frac{1}{T} \int_0^T F \omega x_{\text{load}} dt = \frac{F^2}{2(D_p + D_{em})}; \quad P_{\text{elec}} = D_{em} \frac{F^2}{2(D_p + D_{em})^2};$$

$$P_l = D_{em} \frac{F^2}{2(D_p + D_{em})^2} \frac{R_l}{R_c + R_l}.$$

The electromagnetic damping was calculated from the FEA simulations and the parasitic damping was calculated from the measured total quality factor using the following formula:

$$D_{em} = \frac{N^2 \left(\frac{d\phi}{dx} \right)^2}{R_c + R_l}, \quad D_p = \frac{m\omega_n}{Q_T} - D_{em}$$

The measured total quality factor (total damping factor) and the open circuit quality factor (parasitic damping factor) for 20mg acceleration were 119 (0.0084) and 232 (0.0041), respectively. The calculated electromagnetic damping factor was 0.0043. It can be seen from Figure 49 that the simulated power agrees with the measured power. It is also indicated from the measured quality factor that the maximum power is transferred to the load when the electromagnetic damping and the parasitic damping are equal which agrees with the theoretical model. In this generator, the measured results showed that the generated mechanical and electrical power varied with the square of the acceleration due to no variation of the parasitic damping factor. This is in contrast to the measured results for the macro scale generator, where it was found that the parasitic damping could change with the acceleration level.

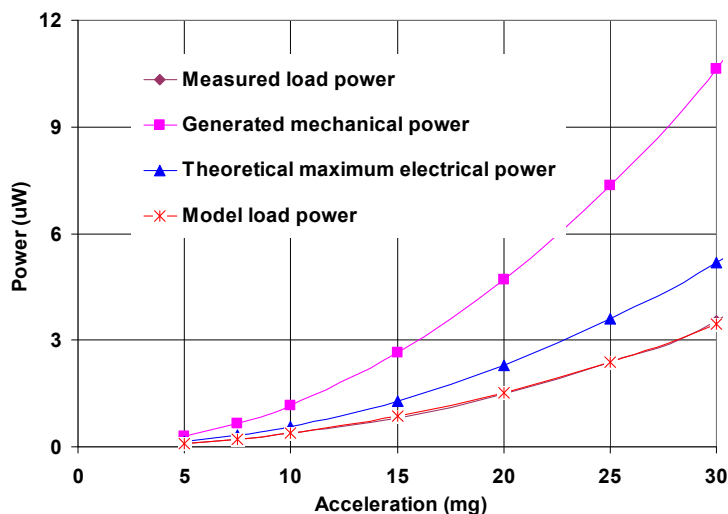


Fig. 49. Measured and calculated power of optimized micro generator for 600 turns coil.

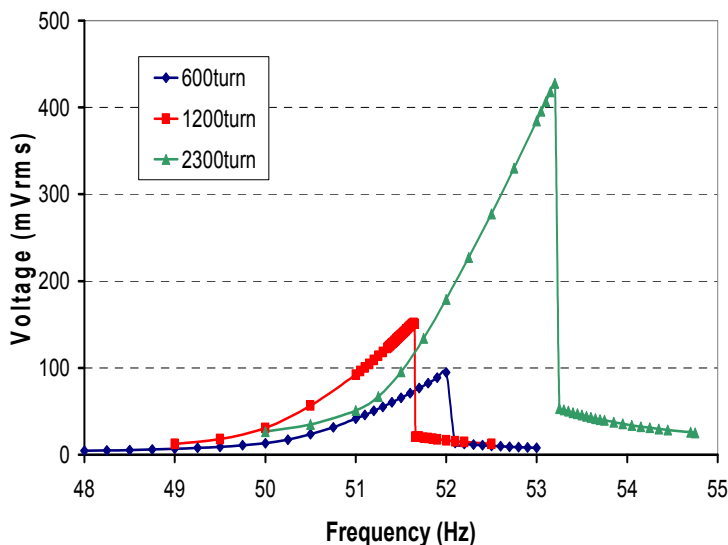


Fig. 50. Measured load voltages on optimum load resistances.

The voltages and power for 600 turn, 1200 turn and 2300 turn generators were also measured at 60 mg acceleration and with different load resistances. Figures 50 & 51 shows the measured load voltage and load power vs frequency on optimum load resistances for each generator. The optimum load resistance for 600 turns, 1200 turns and 2300 turns generators were 200Ω , 500Ω , and $4\text{ k}\Omega$ respectively. The measured voltage shows that the generated voltages are almost proportional to the number of turns. However, the maximum load powers are constant for the three coils due to the nature of wire-wound coil

technology. The measured results could not be analysed with the linear modeling approach due to the non linear behaviour of the generator for this acceleration. These non-linear results could be verified with the non-linear mass-damper- spring theory [30]. However, it is necessary to know the non linear spring constant to verify non-linear theory and this is beyond the scope of this work. Note that for practical operation it may be desirable to operate slightly away from the exact resonance frequency because of this non-linear effect.

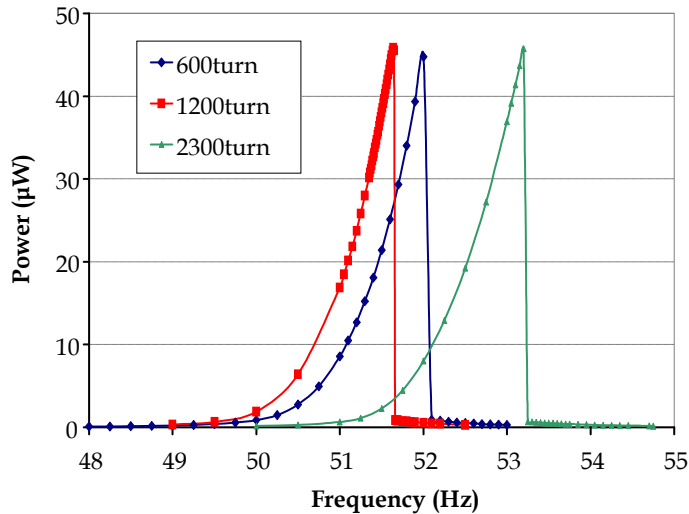


Fig. 51. Measured load powers on optimum load resistances.

2.6 Conclusions

We have presented the theory behind the modeling of the electromagnetic linear vibrational generator. The model for an electromagnetic-based vibrational energy-harvesting device has been compared to measurements on macro scale devices and FE simulation results in order to verify the modeling approach. The optimum conditions observed from measurements are shown to agree well with the model. The model and the experimental results clearly show that the generated mechanical and electrical power depends on the applied force which is the product of mass and acceleration and the damping factor: parasitic and electromagnetic damping. The parasitic damping depends on material properties, acceleration, etc., and the electromagnetic damping depends on parameters of the magnet and coil parameters. The experimental results suggest that significant parasitic damping is always present and that a maximum of 50 % of the generated electrical power could be lost in the coil's internal resistance if the parasitic damping is much greater than the electromagnetic damping. The measured results also indicate that this parasitic damping is not constant with changing acceleration level and most likely it increases with increasing the acceleration level. However in general the exact behaviour of parasitic damping with acceleration will depend on the spring material. The measured results also showed that if the magnet and coil parameters are chosen so as to maximize flux gradient and the electromagnetic damping can be made equal to the parasitic damping, then typically 80-90% of the generated electrical power can be delivered to the load. It is also clear that the generator size depends strongly

on the desired system resonance frequency which in turn depends on the spring constant and the mass attached to the beam. In order to design the generator to operate at less than 10 Hz frequency, the generator should be at least a few cm size generator is size. We introduced the structure of a magnetic spring electromagnetic generator which could be beneficial over the cantilever structure for random human body activity. The prototype generators generated 0.3 - 2.46 mW when placed inside a rucksack which was worn during walking and slow running. These results indicate that a useful amount of voltage and power could be generated from the vibration of the human body. However, this device has not been optimized. The generated power of the magnetic spring generator could be increased by adding a separate coil close to the top or bottom end of the tube and connecting all coil terminals in parallel to the load. Moreover, it is possible that this generator could deliver more energy during walking if placed in other locations on the body such as the waist where higher acceleration level may be available.

3. References

- [1] C. B. Williams, M.A. Harradine Shearwood, P. H. Mellor, T.S. Birch and R. B. Yates, "Development of an electromagnetic micro-generator", IEE Proc. Circuits Devices Systems, vol 148, 337-342, 2001.
- [2] T. V. Buren, "Body-Worn Inertial Electromagnetic Micro-Generators" Ph.D thesis, Swiss Federal Institute of Technology Zurich.
- [3] N. G. Stephen, "Energy harvesting from ambient vibration", Journal of Sound and Vibration, vol 293, 409-525, 2006.
- [4] C. R. Saha, T. O'Donnell, N. Wang and P. McCloskey, "Electromagnetic generator for harvesting energy from human motion", Sensors and Actuators -A: Physical, Volume 147, Issue1, 15 September 2008.
- [5] S. P. Beeby, R. N. Torah, M. J. Tudor, P. Glynne-Jones, T. O'Donnell, C.R. Saha and S. Roy "Micro electromagnetic generator for vibration energy harvesting", Journal of Micromechanics and Microengineering, 17, 1257-1265, 200
- [6] C. Saha, T. O'Donnell, H. Loder, S. Beeby and J. Tudor, "Optimization of an Electromagnetic Energy Harvesting Device", IEEE Transaction on Magnetics, Volume 42, No 10, October 2006.
- [7] T. O'Donnell, C. Saha, S. Beeby and J. Tudor, "Scaling Effects for Electromagnetic Vibrational power Generator", Journal of Microsystem Technology, November, 2006.
- [8] P. D. Mitcheson, T. C. Green, E. M. Yeatman and A. S. Holmes, "Architectures for vibration-driven micro power generators", IEEE/ASME Journal of Microelectromechanical System, Vol 13, no. 3, 429-440, 2004.
- [9] S. Roundy, P.K. Wright and J. Rabaye, "A study of low level vibrations as a power source for wireless sensor nodes", Computer Communication, vol 26, 1131-1144, 2003.
- [10] P. Miao, A.S. Holmes, E.M. Yeatman and T.C. Green, "Micro-machined variable capacitors for power generation", Department of electrical and electronics engineering, Imperial college London, UK.
- [11] G. Despesse, J.J. Chaillout, T. Jager, J.M. Leger, A. Vassilev, S. Basrour and B. Charlot, "High Damping Electrostatic System for Vibration Energy Scavenging", Joint sOc-EUSAI conference, Grenoble October 2005.
- [12] P. Mitcheson, Stark B, P. Yeatman E, Holmes A and Green T, "Analysis and optimisation of MEMS on-chip power supply for self powering of slow moving sensors", Proc. Eurosensors XVII.

- [13] F. Peano and T. Tambosso "Design and optimization of a MEMS electret-based capacitive energy scavenger" *Microelectromechanical Systems*, Journal of Volume 14, Issue 3, June 2005 Page(s):429 – 435.
- [14] <http://www.physicsclassroom.com/class/energy/u5l1c.cfm>
- [15] *Transformer and Inductor Design Handbook*, Colonel W.T. McLyman, Second Edition, Marcel Dekker Inc. New York, 1988.
- [16] *Electromagnetic and Electromechanical machine*, Leander W. Matsch, and J. Derald Morgan, Third Edition, John Wiley and Sons.
- [17] *Electromechanics and Electric Machines*, S. A. Nasar and L.E. Unnewehr, Second Edition, John Wiley and Sons.
- [18] F. Bancel "Magnetic nodes", *Journal of Physics D: Applied physics* 32 (1999), 2155-2161.
- [19] http://services.eng.uts.edu.au/cepe/subjects_JGZ/eet/eet_ch4.pdf
- [20] John Borwick, *Loudspeaker and Headphone Handbook*, Focal press, Second edition
- [21] P. Glynne-Jones, M. J. Tudor, S. P. Beeby, N.M. White, "An electromagnetic vibration powered generator for intelligent sensor systems", *Sensors and Actuators A*, 110 (2004).
- [22] X. Zhang and W. C. Tang, "Viscous air damping in laterally driven microresonators", *IEEE proceedings on MEMS workshop*, pp. 199-204, 1994
- [23] *Thermoelastic damping in micro and nanomechanical systems*, R Lifshitz, M Roukes, *Physical Review B*, Vol. 61, No. 8, 15 Feb 2000, pp.5600-5609.
- [24] *Internal friction in solids: 1: theory of internal friction in reeds*, C Zener, *Physical Review*, Vol. 52, 1937, pp. 230-235.
- [25] *An analytical model for support loss in micromachined beam resonators*, Z Hao, A Erbil, F Ayazi, *Sensors and Actuators A*, Vol. 109, 2003, pp. 156-164.
- [26] *Energy dissipation in sub-micrometer thick single crystal silicon cantilevers*, J Yang, T Ono, M Esashi, *J. Micromech. Systems*, Vol. 11, No. 6, 2002, pp.775-783.
- [27] Andrew D. Dimarogonas, Sam Haddad, *Vibration for engineering*, Prentice-Hall International editions, chapter 12, page 605.
- [28] R. Scott Wakeland, "Use of electrodynamic drivers in thermo-acoustic refrigerators", *Journal of Acoustical Society of America*, 107(2), February 2000.
- [29] Z. Yu, S. Backhaus and A. Jaworski, "Design and testing of a travelling wave looped tube engine for low cost electricity generators in remote and rural areas", *American Institute of Aeronautics and Astronautics*, 2009.
- [30] Ali H. Nayfeh, Dean T. Mook, *Nonlinear Oscillation*, A Wiley-interscience publication.
- [31] T. von Buren, P. Lukowicz and G. Troster, "Kinetic Energy Powered Computing-an Experimental Feasibility Study", *Proc. 7th IEEE Int. Symposium on Wearable Computer*.
- [32] T. Starner and J. A. Paradiso, "Human generated power for mobile electronics", *Low Power Electronics Design*, CRC Press, Summer 2004.
- [33] *Vibrational Energy Scavenging (VIBES)*, FP6-IST-507911, Deliverable: Application Analysis and Specification, June 2004.
- [34] A. Luzy. 1472335: magneto flash light. US Patent, October 30, 1923.
- [35] S. C. Mukhopadhyay, J. Donaldson, G. Sengupta, S. Yamada, C. Chakraborty and D. Kacprzak, "Fabrication of a repulsive-type magnetic bearing using a novel arrangement of permanent magnets for vertical-rotor suspension", *IEEE Transactions on Magnetics*, vol. 39, No. 5, September 2003.
- [36] N. B. Bharatula, S. Ossevoort, M. Stager, G. Troster, "Towards Wearable Autonomous Microsystems", *Pervasive computing, proceeding of the 2nd international conference*, page 225-237, Vienna, Austria, April 2004.



Sustainable Energy Harvesting Technologies - Past, Present and Future

Edited by Dr. Yen Kheng Tan

ISBN 978-953-307-438-2

Hard cover, 256 pages

Publisher InTech

Published online 22, December, 2011

Published in print edition December, 2011

In the early 21st century, research and development of sustainable energy harvesting (EH) technologies have started. Since then, many EH technologies have evolved, advanced and even been successfully developed into hardware prototypes for sustaining the operational lifetime of low-power electronic devices like mobile gadgets, smart wireless sensor networks, etc. Energy harvesting is a technology that harvests freely available renewable energy from the ambient environment to recharge or put used energy back into the energy storage devices without the hassle of disrupting or even discontinuing the normal operation of the specific application. With the prior knowledge and experience developed over a decade ago, progress of sustainable EH technologies research is still intact and ongoing. EH technologies are starting to mature and strong synergies are formulating with dedicate application areas. To move forward, now would be a good time to setup a review and brainstorm session to evaluate the past, investigate and think through the present and understand and plan for the future sustainable energy harvesting technologies.

How to reference

In order to correctly reference this scholarly work, feel free to copy and paste the following:

Chitta Ranjan Saha (2011). Modelling Theory and Applications of the Electromagnetic Vibrational Generator, Sustainable Energy Harvesting Technologies - Past, Present and Future, Dr. Yen Kheng Tan (Ed.), ISBN: 978-953-307-438-2, InTech, Available from: <http://www.intechopen.com/books/sustainable-energy-harvesting-technologies-past-present-and-future/modelling-theory-and-applications-of-the-electromagnetic-vibrational-generator>

INTECH
open science | open minds

InTech Europe

University Campus STeP Ri
Slavka Krautzeka 83/A
51000 Rijeka, Croatia
Phone: +385 (51) 770 447
Fax: +385 (51) 686 166
www.intechopen.com

InTech China

Unit 405, Office Block, Hotel Equatorial Shanghai
No.65, Yan An Road (West), Shanghai, 200040, China
中国上海市延安西路65号上海国际贵都大饭店办公楼405单元
Phone: +86-21-62489820
Fax: +86-21-62489821